# ELECTROMECHANICAL MODELING AND OPEN-LOOP CONTROL OF PARALLEL-PLATE PULSED PLASMA MICROTHRUSTERS WITH APPLIED MAGNETIC FIELDS

By

David Daniel Laperriere

A Thesis

Submitted to the Faculty

of the

WORCESTER POLYTECHNIC INSTITUTE

in partial fulfillment of the requirements for the

Degree of Master of Science

in

Mechanical Engineering

by
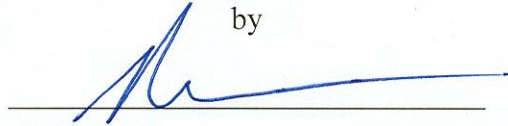
June, 5 2005

APPROVED:

Dr. Nikolaos A. Gatsonis, Advisor

Associate Professor, Mechanical Engineering Department
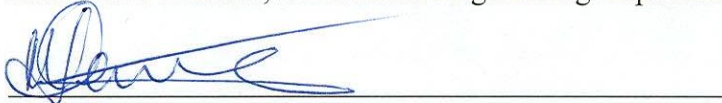
Dr. Michael Demetriou, Co-Advisor

Associate Professor, Mechanical Engineering Department
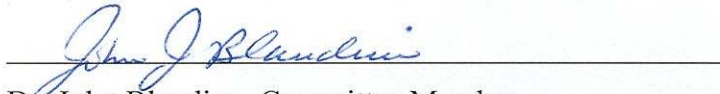
Dr. John Blandino, Committee Member

Assistant Professor, Mechanical Engineering Department
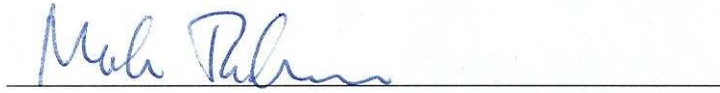
Dr. Mark Richman, Graduate Committee Representative

Associate Professor, Mechanical Engineering Department

**Abstract**

The pulsed plasma thruster (PPT) is an onboard electromagnetic propulsion device currently being considered for use in various small satellite missions. The work presented in this thesis is directed toward improving PPT performance using a control engineering approach along with externally applied magnetic fields. An improved one dimensional electromechanical model for PPT operation is developed. This slug model represents the PPT as an LRC circuit with a dynamics equation for the ablated plasma. The improved model includes detailed derivation for the induced magnetic field and a model for the plasma resistance. A modified electromechanical model for the case of externally applied magnetic fields is also derived for the parallel plate geometry. A software package with a graphical user interface (GUI) is developed for the simulation of various PPT types, geometric configurations, and parameters The simulations show excellent agreement with data from the Lincoln Experimental Satellite (LES)-6, the LES-8/9 PPT and the Univ. of Tokyo PPT. The control objective employed in this thesis involves the maximization of the specific impulse and thrust efficiency of the PPT, which are each directly related with the exhaust velocity of the thruster. This objective is achieved through the use of an externally applied magnetic field as a system actuator. To simulate an open-loop constant-input controller the modified electromechanical PPT model is applied to the various PPT configurations. In this controller the external magnetic field was applied as constant throughout or portions of the PPT channel. For the Univ. of Tokyo PPT a magnetic field applied over the entire 6-cm long channel increases the specific impulse and thrust efficiency by 10% over the case that the filed is applied in the first 1.75 cm of the PPT channel. The magnitude of these increases

compare well with the results of the UOT applied B-field experiments.    For the LES-6

and LES-9 PPTs, the simulations predicts significant performance enhancements with

approximately linear increases for the specific impulse, thrust efficiency and impulse bit.

# Table of Contents

# List of Figures

# List of Tables

# Nomenclature

| Symbol | Definition ( SI Units ) |
|---|---|
| $A$ | Current sheet cross sectional area ($m^2$) |
| $\mathbf{A}$ | Area vector ($m^2$) |
| $b$ | Kinetic theory mass distribution coefficient ($m^{-1}$) |
| $\bar{b}_0$ | Impact parameter (m) |
| $\mathbf{B}$ | Total magnetic field vector (T) |
| $B_{ext}$ | Externally applied magnetic field (T) |
| $\mathbf{B}_{ind}$ | Magnetic field vector due to PPT circuit self-inductance (T) |
| $B_{\phi}$ | Azimuthal self-induced magnetic field (T) |
| $c_f$ | Dynamic model damping term (N s $m^{-1}$) |
| $C$ | Capacitance (F) |
| $e$ | Electron charge (C) |
| $E_0$ | Energy stored on capacitor at $t = 0$ (J) |
| $E_c$ | Energy stored on capacitor (J) |
| $E_B$ | Energy stored in magnetic field (J) |
| $E_{\Omega}$ | Energy dissipated in ohmic heating (J) |
| $E_{KE}$ | Kinetic energy of current sheet (J) |
| $\mathbf{f}$ | Drift vector field |
| $\mathbf{F}$ | Total force vector acting on current sheet |
| $\mathbf{F}_{ind}$ | Total Lorenz force due to self-inductance field (N) |
| $F_L$ | Lorentz force (N) |
| $g$ | Acceleration due to gravity at sea level, 9.81 (m $s^{-2}$) |

| | |
|---|---|
| **g** | Input vector field |
| $\bar{g}$ | Photon momentum density (kg m s$^{-1}$) |
| $h$ | Distance between electrodes in parallel plate geometry (m) |
| $I$ | Current (A) |
| $I_{bit}$ | Impulse bit (N s) |
| $I_{sp}$ | Specific impulse (s) |
| **j** | Current density field vector (A m$^{-2}$) |
| $k$ | Boltzman constant, 1.3807e$^{-23}$ (J K$^{-1}$) |
| $K$ | Thermal conductivity of electron gas (W m$^{-1}$ K$^{-1}$) |
| **K** | Surface current density vector (A m$^{-1}$) |
| $K_i$ | Surface current density (A m$^{-1}$) |
| $(KE)_e$ | Kinetic energy at exhaust (J) |
| $l$ | Channel length (m) |
| $L$ | Inductance (H) |
| $L_0$ | Inductance at $t = 0$ (H) |
| $L_c$ | Internal inductance of the capacitor (H) |
| $L_{ce}$ | Inductance due to current sheet moving down coaxial electrodes (H) |
| $L'_{ce}$ | Inductance per unit channel length for coaxial geometry (H m$^{-1}$) |
| $L_e$ | Inductance due to wires and leads (H) |
| $L_{pe}$ | Inductance due to current sheet moving down parallel plate electrodes (H) |
| $L'_{pe}$ | Inductance per unit channel length for parallel plate geometry (H m$^{-1}$) |
| $L_T$ | Total circuit inductance (H) |
| $m$ | Mass of current sheet (kg) |
| $m'$ | Mass per unit length (kg m$^{-1}$) |
| $m_0$ | Mass of current sheet at $t = 0$ (kg) |
| $m_e$ | Mass of current sheet at exhaust (kg) |
| $\dot{m}_f$ | Propellant flow rate (kg s$^{-1}$) |

| | |
|---|---|
| $m_i$ | Ion mass (kg) |
| $m_t$ | Total mass accumulated in current sheet during discharge (kg) |
| $M$ | Final spacecraft mass (kg) |
| $M_0$ | Initial spacecraft mass (kg) |
| $n$ | Particle number density (m$^{-3}$) |
| $\mathbf{n}$ | Area normal vector |
| $n_0$ | Neutral number density (m$^{-3}$) |
| $n_e$ | Electron density (m$^{-3}$) |
| $\bar{p}$ | Particle momentum density (kg m s$^{-1}$) |
| $P$ | Power delivered to circuit (J s$^{-1}$) |
| $P_f$ | Fraction of ionization and excitation accomplished at the expense of the plasma thermal energy |
| $\bar{\bar{P}}$ | Particle stress tensor (N m$^{-2}$) |
| $Q$ | Charge on capacitor (C) |
| $r$ | Radial distance (m) |
| $r_i$ | Radius of inner electrode for coaxial geometry (m) |
| $r_o$ | Radius of outer electrode for coaxial geometry (m) |
| $R$ | Resistance ($\Omega$) |
| $R_0$ | Capacitor, wire and lead resistance ($\Omega$) |
| $R_c$ | Capacitor resistance ($\Omega$) |
| $R_e$ | Wire and lead resistance ($\Omega$) |
| $R_{pe}$ | Electrode resistance ($\Omega$) |
| $R_p$ | Plasma resistance ($\Omega$) |
| $R_T$ | Total circuit resistance ($\Omega$) |
| $S$ | Wall area (m$^2$) |
| $S_i$ | Electron-neutral collision term (m$^3$ s$^{-1}$) |
| $t$ | Time (s) |

| | |
|---|---|
| $t_{el}$ | Electrode thickness for parallel plate geometry (m) |
| $T$ | Plasma temperature (K) |
| $\bar{\bar{T}}$ | Maxwell stress tensor (N m$^{-2}$) |
| $T_e$ | Electron temperature (K) |
| $T_F$ | Thrust (N) |
| $V$ | Velocity (m s$^{-1}$) |
| $V_0$ | Voltage across capacitor at $t = 0$ (V) |
| $V_c$ | Voltage drop across capacitor (V) |
| $w$ | Width of electrodes in parallel plate geometry (m) |
| $W$ | Work (J) |
| $x_1$ | Position state variable (m) |
| $x_2$ | Charge on capacitor state variable (C) |
| $x_3$ | Velocity state variable (m s$^{-1}$) |
| $x_4$ | Current state variable (A) |
| $\dot{x}_e$ | Current sheet exhaust velocity (m s$^{-1}$) |
| $\mathbf{x}_s$ | Position vector of current sheet measured at the trailing edge of the current sheet (m) |
| $\mathbf{x}_{st}$ | State vector |
| $x_s$ | Position of current sheet measured at the trailing edge of the current sheet (m) |
| $z$ | Charge number |
| | |
| $\alpha$ | Mass distribution loading parameter |
| $\alpha_2$ | Two body recombination rate coefficient (m$^3$ s$^{-1}$) |
| $\alpha_3$ | Three body recombination rate coefficient (m$^6$ s$^{-1}$) |
| $\Gamma$ | Particle diffusion current (s$^{-1}$) |
| $\delta$ | Current sheet thickness (m) |

| | |
|---|---|
| $\eta_t$ | Thrust efficiency |
| $\Lambda$ | Lamda parameter |
| $\lambda_{PPT}$ | Total magnetic flux through PPT circuit (T m$^{-2}$) |
| $\lambda_c$ | Flux linkage through capacitor (T m$^{-2}$) |
| $\lambda_e$ | Flux linkage through wires and leads (T m$^{-2}$) |
| $\lambda_{pe}$ | Flux linkage through the plate electrodes (T m$^{-2}$) |
| $\lambda_D$ | Debye length (m) |
| $\lambda_y$ | Total magnetic flux through magnetic yoke (T m$^{-2}$) |
| $\mu_0$ | Magnetic permeability of free space, 1.2566e$^{-6}$ (Wb A$^{-1}$ m$^{-1}$) |
| $\sigma$ | Conductivity ($\Omega^{-1}$ m$^{-1}$) |
| $\sigma_p$ | Plasma conductivity ($\Omega^{-1}$ m$^{-1}$) |
| $\tau$ | Characteristic pulse time (s) |
| $\Phi_1$ | Ionization-excitation potential per ion (V) |
| $\Phi_2$ | Excitation loss rate parameter (V s$^{-1}$) |

# Chapter 1

# Introduction

## 1.1.    Pulsed Plasma Thrusters and Microspacecraft

There is ongoing interest in the development of increasingly smaller, compact satellites, in particular, for fleets or constellations of satellites to be used in current and future missions. These missions, ranging from space-based interferometry to Department of Defense radar and surveillance [Rayburn et al., 2005], could rely upon microspacecraft with wet masses less than 100 kg [Mueller, 2000]. Evidence of microspacecraft interest are the various programs that have been initiated by government and military institutions intent on the development of microsatellite technology. The Air Force, for example, has shown interest through its TechSat21 and University Nanosatellite Programs. The TechSat21 program is intent on demonstrating the cost and functionality benefits of replacing current large satellite system architecture with distributed networks of small satellites [Cobb, 1999]. The University Nanosatellite program, has the goal of design, fabrication and functional testing of small satellites [Campbell et al., 1999]. One of the initial products of this program is the Ionospheric Observation Nanosatellite Formation (ION-F). The operational goals of this three satellite formation are ionosphere science measurements and a demonstration of formation flying [Campbell et al., 1999]. Integral to the success of microsatellites flying in formation are the propulsion systems used to maintain the relative positions of the spacecraft. In the case of the ION-F micro

satellites, an electric prolusion device, the micro pulsed plasma thruster (μPPT), with its small discrete forces and overall fuel efficiency, was chosen to satisfy this requirement. This device was chosen above other competing thrusters (e.g. cold gas thruster) due to comparative mass savings benefits and its robust simplicity.

The significant advantages electric thrusters hold over their chemical counterparts has led to such experiments as the Air Force Research Laboratory's (AFRL) current Microsatellite Propulsion Integration (MPI) mission. The objective of this experiment is to "demonstrate greatly improved microsatellite maneuverability with low power electric propulsion" [Johnson, et al., 2003]. It is certainly apparent from this abundance of development and commitment that the market for electric propulsion, particularly for use on small satellites, is on a continual rise.

The advantage electric propulsion has over chemical propulsion is a result of the thrust production mechanism. Chemical propulsion relies solely upon gas dynamic forces and effects for propellant acceleration. In contrast, electric propulsion technologies, such as ion thrusters, Hall thrusters, colloid thrusters and pulsed plasma thrusters (PPT), also have an electrostatic or an electromagnetic force component acting on ionized propellant. The effective result of this difference is electric thrusters tend to have exhaust velocities orders of magnitude greater than their chemical counterparts. A quantification of the advantage of EP over chemical propulsion is found in the specific impulse of the thrusters, defined as

$$I_{sp} = \frac{T_F}{\dot{m}_f g}. \tag{2.1}$$

where $T_F$ is the thrust, $\dot{m}_f$ is the propellant mass flow rate and $g$ is the acceleration of gravity. While chemical thrusters have exhaust velocities and specific impulses upwards

of 4 km/s and 350 s, electric propulsion devices have exhaust velocities exceeding 30 km/s with specific impulses often greater than 1000 s. For given missions velocity requirements, $\Delta V$, the "rocket equation" is

$$\Delta V = gI_{sp} \ln\left(\frac{M_0}{M}\right), \qquad (2.2)$$

where $M_0$ is the initial spacecraft mass and $M$ is the spacecraft mass after thruster firing. Therefore, the increase in specific impulse results in less propellant mass being needed for a given mission $\Delta V$.

While electric thrusters are more fuel efficient, this comes at an expense to the instantaneous thrust level of these devices. Electric thrusters generate little more than a few Newton's of thrust, with many types of electric propulsion devices producing no more than a few milli-Newton's of thrust. Because of this, electric propulsion devices are not suited for quick spacecraft maneuvers, such as orbit-raising on the order of hours or days. However, for deep space exploration and a plethora of maneuvers; such as station keeping, attitude control, slow orbit modifications and formation control, electric thrusters continue to be the candidate of choice [Gagne, 2000].

Electric propulsion devices can be divided into several categories based on the acceleration process involved: electrothermal, electrostatic, and electromagnetic. PPTs are a form of electromagnetic propulsion, which has been in and around the industry limelight for much of the history of electric propulsion. PPTs began to be developed during the late 1950's in facilities in Russia and the United States as a product of early thermonuclear fusion experiments [Jahn et al., 2002]. Though PPT interest and development reached a pinnacle in the mid 1960's with several devices being flown on

spacecraft, by 1970 much of the early interest waned. In recent years, however, due to the growing importance of small and micro-satellites, a renewed interest in PPTs has arisen.

There are several types of PPTs currently under investigation. They are categorized by the geometry of the electrodes and the propellant being utilized. The electrode configurations are coaxial (Figure 1.1) or parallel plate (Figure 1.2) and the propellants are gas or ablated solid.
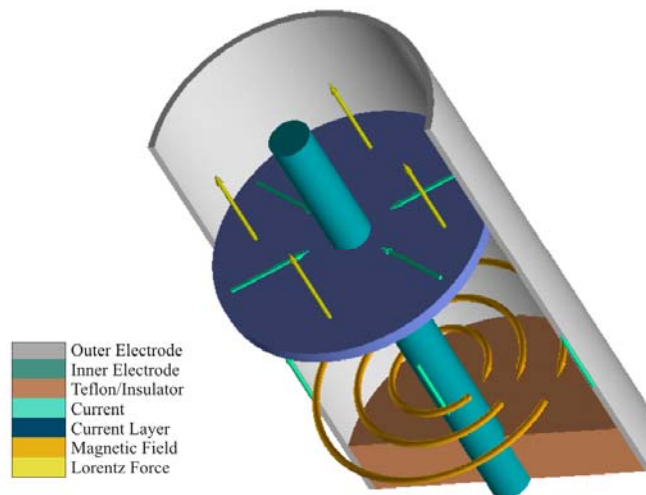


**Figure 1.1  Coaxial PPT cutaway.**

Anode Plate Electrode
Cathode Plate Electrode
Teflon/Insulator
Current
Current Layer
Magnetic Field
Lorentz Force
Capacitor
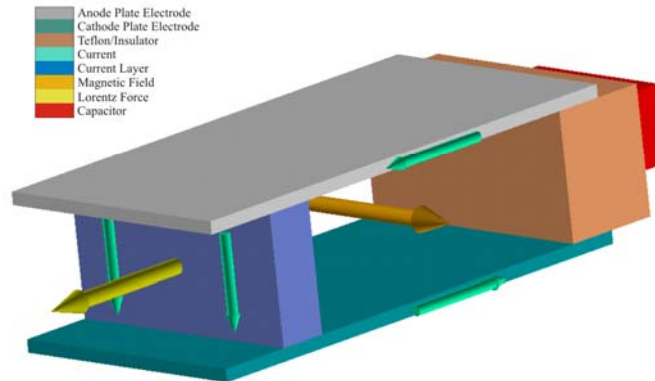
**Figure 1.2  Parallel plate PPT.**

The gas-fed PPT (GFPPT) utilizes a gas for propellant, with the noble gasses (e.g. xenon and argon) most often being used.  It consists of a gas storage device, a gas inlet, two electrodes spaced to form a channel, a sparking device and a main energy storage capacitor.  Historically, GFPPT required the use of fast acting valves; however, recent developments of pulsing schemes for GFPPT have eliminated this need [Ziemer et al., 1997].  The sparking device is embedded in one of the plates as a means to initiate the gas ionization.  Once an initial ionization is accomplished the main capacitor is discharged across the electrodes.  This creates an approximately axially symmetric current sheet at the surface of the insulator.  With current flowing through the complete PPT circuit, a self-magnetic field is produced.  This magnetic field interacts with the current sheet by accelerating it through a $\mathbf{j} \times \mathbf{B}$ Lorentz force.  The direction of this force is to increase the area of the PPT circuit loop.  This electromagnetic force coupled with gas dynamic forces act to accelerate the relatively dense current sheet entraining the neutral gas further up the channel as it exits the thruster.

An ablative PPT utilizes a solid (generally Teflon) for propellant. It consists of a spring fed piece of Teflon at the back a thruster channel, the two electrodes that form the channel, a sparking device and a main energy storage capacitor. The sparking device is located at the back of the thruster channel ensuring the creation of a current sheet along the Teflon face. Once the sparking device is fired, the main capacitor is discharged. The thermal flux and particle bombardment from the current ablates and ionizes a small amount of the solid. With current flowing through the complete PPT circuit, a self-magnetic field is produced. This magnetic field interacts with the current sheet by a $\mathbf{j} \times \mathbf{B}$ Lorentz force as to increase the area PPT circuit loop. This force coupled with the gas dynamic expansion forces accelerate the current sheet out of the thruster at velocities upwards of 40 km/s [Vondra, 1970].

The beginnings of the PPT can be traced back to thermonuclear fusion programs conducted in the United States and Russia during the 1950s. A derivative of these programs was a family of plasma accelerators closely related to the GFPPT [Jahn et al., 2002]. With these accelerators being modified for propulsion configuration, by the early 1960s both Russia and the United States had developed the first PPT systems [Jahn et al., 2002]. The first flight-tested electric propulsion device was a Russian PPT flown on the Zond-2 spacecraft in 1964 providing three-axis attitude control [Pollard et al, 1993]. For several years after this first flight, development and testing continued in both Russia and the United States resulting in the United States successfully flying PPTs on the LES-6 satellite for station keeping purposes. This early PPT work also resulted in several other PPT thruster, notably the LES-8/9. Figure 1.3 shows a recent derivative of the LES-8/9, the NASA Goddard Research Center (GRC) Laboratory PPT. This laboratory PPT was

utilized in experimental and modeling investigation as summarized in Gatsonis et al (2001).
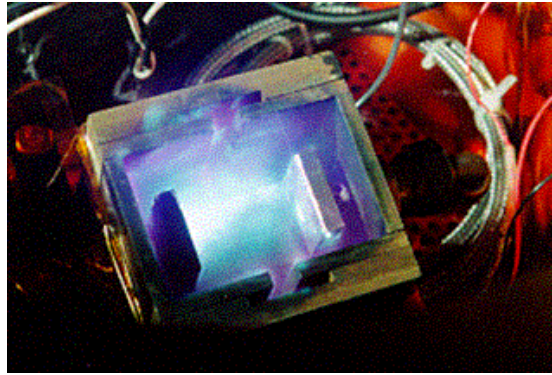


**Figure 1.3  NASA GRC Laboratory PPT firing.**

Despite the early successes with providing secondary propulsion, the majority of the electric propulsion research throughout the 1970s was directed at producing primary propulsion systems for large satellites.  With only GFPPTs able provide the required level of thrusting, PPT researchers ran into engineering limitations.  These limitations were with the massive capacitors and the lifetime requirements of fast-acting valves needed to achieve high propellant mass utilization.  As a result of these issues, by 1975, research and development of GFPPTs waned [Pollard et al., 1993].  PPT research did continue on at much diminished rate as the APPT was utilized as a secondary propulsion system on a series of U.S. Navy satellites and in several experiments independently conducted by China and the United States [Jahn et al., 2002].

Despite these flights, PPT research remained relatively dormant until the mid-1990s when the development of power-limited satellites was initiated by an interest in formations and constellations of small satellites.  With improved capacitor technology, the APPT was looked upon as a leading contender for a plethora of attitude control and station keeping maneuvers on these low power satellites.  This rekindled APPT

development has also sparked renewed interest in the GFPPT.  Recent developments in pulsing schemes have eliminated the need for fast-acting valves in GFPPTs.  These recent developments have once again brought the PPT back into the limelight of spacecraft technology.

## 1.2.    Review of PPT Electromechanical Modeling

Much research has been conducted at various industrial and academic facilities to improve the design and performance characteristics of the PPT.  In particular, a significant amount of theoretical modeling has been performed ranging from low-order one dimensional models [Jahn, 1968] to advanced MHD modeling [Mikellides, 1998]. This section specifically addresses the low-order slug/snowplow modeling that has been performed.  In the modeling review, the various one-dimensional electromechanical models that have been derived and employed in the analysis and optimization of parallel-plate and coaxial PPTs are addressed.  These models are listed chronologically; however, due to the great amount of previous work performed in this area, only models containing unique advances over previous modeling efforts are listed.

### 1.2.1.  Parallel-Plate PPT

The development of a simple one-dimensional mathematical model of parallel plate PPT operation first appears in Jahn [1968].  It appears along with several other heuristic models aimed at describing unsteady electromagnetic acceleration.  In this model the acceleration process and circuit components of the PPT are modeled as a dynamical system interacting with an electrical system, that is, as an electromechanical system.
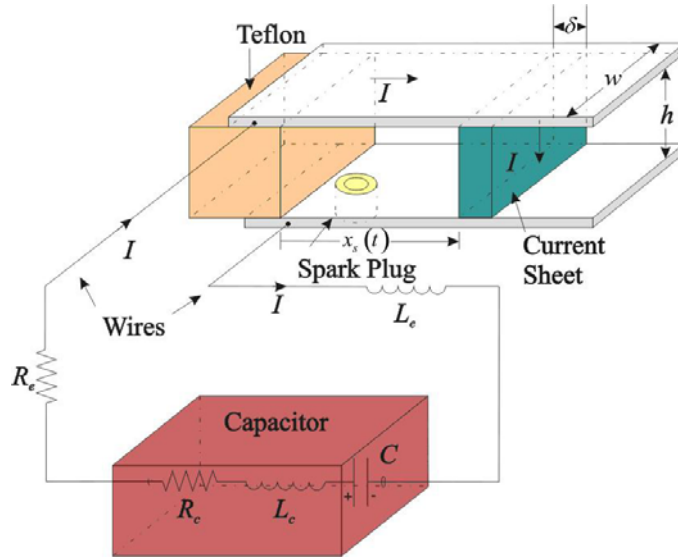
**Figure 1.4  Parallel plate PPT components.**

The parallel plate PPT (shown in Figure 1.4) operates electrically as an LRC circuit (Figure 1.5).
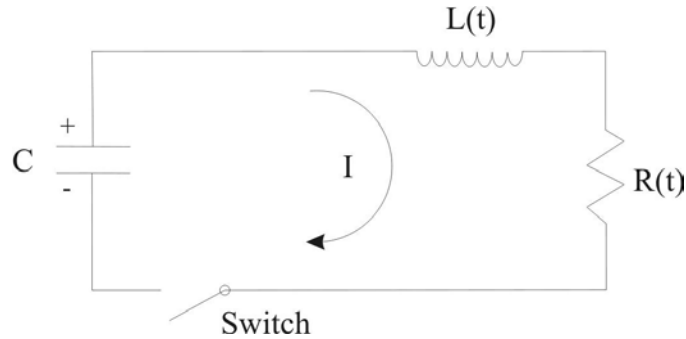


**Figure 1.5  Simplified electric circuit diagram.**

Accordingly, Jahn modeled the electrical system with the following circuit equation

$$V_c + \frac{d}{dt}(LI) + RI = V_0 - \frac{1}{C}\int_0^t I(\tau)\,d\tau + \frac{d}{dt}\Big[\big(L_0 + L'_{pe}x_s\big)I\Big] + RI = 0. \tag{2.3}$$

where $V_c$, $L$, $I$, $V_0$, $C$, $L_0$, $L'_{pe}$, $x_s$ and $R$ are, respectively, the voltage across the capacitor, total circuit inductance, circuit current, initial voltage, capacitance, initial inductance, inductance per unit length for parallel plate electrodes, current sheet position

9

(measured at the trailing edge of the current sheet) and circuit resistance. This equation is a statement of Kirchoff's voltage law for the circuit appearing in Fig 1.5. By approximating the parallel plates as quasi-infinite in width $(w \gg h)$, the parallel plate inductance per unit length, $L'_{pe}$, can be written as

$$L'_{pe} = \mu_0 \frac{h}{w},$$
(2.4)

where $h$, $w$ and $\mu_0$ are, respectively, the distance between parallel plate electrodes, the width of the electrodes and the magnetic permeability. Though the resistance of the plasma, $R_p$, may be time varying in an unknown manner, Jahn lumped it into a constant circuit resistance term $R$. Dynamically, the entire mass in the current sheet was presumed to be accelerated as a single unit or "slug". Under this assumption, Jahn represented the dynamical system of his PPT model through Newton's Second Law as

$$\frac{d}{dt}(m\dot{x}_s) = \frac{1}{2}L'_{pe}I^2,$$
(2.5)

where $m = m_0$, the mass of the current sheet, is taken as being constant throughout the process. The term on the right corresponds to the $\mathbf{j} \times \mathbf{B}$ electromagnetic force acting on the current sheet. In this model the gas dynamic forces acting on the current sheet are presumed to be negligible.

The slug model was used extensively in the investigation of the Lincoln Laboratories LES family of parallel plate PPTs beginning with Waltz [1969] and the LES-6 thruster. The equations in Waltz remain unchanged from Jahn's model with the exception that the conservation of energy for the circuit was utilized instead of the circuit equation (Kirchoff's voltage law). The conservation of energy for the system was found

by expanding the circuit equation, multiplying each term in the circuit equation by $I = -C\dot{V}$ and integrating it with respect to time

$$\frac{1}{2}\left(L_0 + L'_{pe}x_s\right)I^2 + \frac{1}{2}CV_c^2 + \int_0^t \frac{1}{2}L'_{pe}Id\tau + \int_0^t \left(R_0 + R_p\right)I^2d\tau = \frac{1}{2}CV_0^2,\qquad(2.6)$$

where $R_0$ is the resistance due to the capacitor, wires and leads and $R_p$ is the plasma resistance. The terms in (2.6) represent, respectively, the energy stored in the magnetic field, the capacitor energy, the kinetic energy supplied to the slug, ohmic heating losses and the total energy for the system.

An improved electromechanical model appeared in Vondra [1970] in an attempt to improve the LES-6 design. While the circuit equation of this slug model remained unchanged, Vondra made a significant change to the dynamical equation, writing the momentum balance in terms of the Maxwell stress tensor $\bar{\bar{T}}$, the particle stress tensor $\bar{\bar{P}}$, the particle momentum density $\bar{p}$, and photon momentum density $\bar{g}$. Here, the divergence of the Maxwell stress tensor gives the particle electromagnetic force density and the divergence of the particle stress tensor gives the gas dynamic force density. These are related to the particle momentum density and the photon momentum density through the following momentum equation,

$$\iiint \nabla \cdot \left(\bar{\bar{T}} + \bar{\bar{P}}\right)dV + \frac{\partial}{\partial t}\iiint \left(\bar{p} + \bar{g}\right)dV = 0.\qquad(2.7)$$

This equation was simplified through various assumptions and calculus manipulation to,

$$\int_0^t \left(\frac{1}{2}L'_{pe}I^2 + hwnkT\right)dt = m_0\dot{x}_s,\qquad(2.8)$$

whose time derivative is

$$\frac{d}{dt}\left(m_0 \dot{x}_s\right) = \frac{1}{2}L'_{pe}I^2 + hwnkT, \qquad\qquad (2.9)$$

where $k$ is Boltzman's constant, $n$ is the particle number density and $T$ is the plasma temperature. In comparing this equation with previous models it is seen that there is an extra force term acting on the slug. This force models the gas dynamic forces accelerating the slug away from the Teflon face.

The next appearance of a parallel plate APPT slug model was in a thesis aimed at optimizing the LES-8/9 APPT [Leiweke, 1996]. This model is identical to Waltz except that two different inductance models were analyzed. In addition to the original inductance model run in previous work, a specialized "fringe" inductance model was developed. The original model approximated the system by assuming quasi-infinite parallel plate geometry. "Fringe" effects are those effects due to finite parallel plate geometry. The "fringe" inductance model attempted to model these effects under the premise that parallel plate geometries made these effects non-negligible. However, after comparing the results of each model to real LES data it was found that the original inductance model produced more accurate results.

Another attempt to improve on the inductance model was presented by Burton et al [1998]. This model incorporates finite-width and non-zero plate thickness effects of real rectangular parallel plate conductors

$$L_{pe} = \frac{\mu_0}{\pi}\left[\frac{3}{2}x_s + x_s \ln\left(\frac{h}{w+t_{el}}\right) - h + 0.22\left(w+t_{el}\right)\right], \qquad\qquad (2.10)$$

where $t_{el}$ is the plate thickness. Differentiating (2.10) with respect to the current sheet position leads to an inductance per unit length down the channel of the PPT given by

$$L_{pe}^{'} = \frac{\mu_0}{\pi} \left[ \frac{3}{2} + \ln \left( \frac{h}{w + t_{el}} \right) \right].$$
(2.11)

The most recent modification to the parallel plate slug model appears in a paper by Gatsonis and Demetriou [2004]. This work is the first attempt of its kind at utilizing the slug model to develop a feedback controller aimed at optimizing the exhaust velocity of the PPT. The regular integro-differential system of equations is utilized in this model, with the notable exception of damping and control terms being added in the momentum equation. The control term here is assumed to be an externally applied magnetic field,

$$\frac{d}{dt} \left( m\dot{x}_s \right) = \frac{1}{2} L_{pe}^{'} I^2 + IhB_{ext} - c_f \dot{x}_s,$$
(2.12)

where $B_{ext}$ and $c_f$ are, respectively, the external field strength and frictional damping coefficient.

## 1.2.2. Coaxial PPT

The majority of one-dimensional PPT modeling throughout the last 40 years has been developed for coaxial GFPPTs (Figure 2.3). The geometric and operational differences of these thrusters with ablative PPTs call for different one-dimensional models than those utilized in the previously discussed parallel plate PPTs. The appearance of a simple one-dimensional mathematical model of coaxial GFPPT operation first appears in Hart [1962] seven years before the first parallel plate PPT model. Hart developed this model to describe the operating conditions of a predecessor of the coaxial GFPPT; the gas-fed plasma gun.
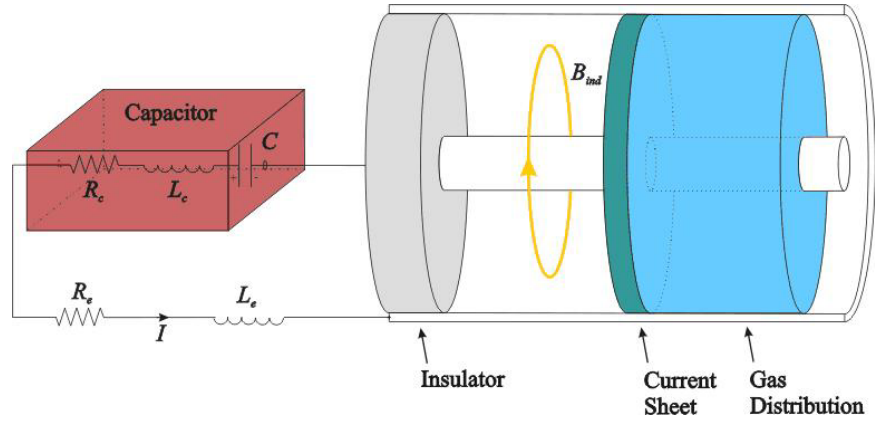
**Figure 1.6  Coaxial GFPPT Components**

This model constitutes the first known appearance of the snowplow model in literature. At first glance there is very little difference between this model and the simple slug models previously discussed.  As for the slug models, Hart's snowplow model was a dynamical system interacting with an electrical system.  The electrical system was modeled as an LRC circuit, shown in Figure 2.4, exactly as it was for the parallel plate PPT with no differences.
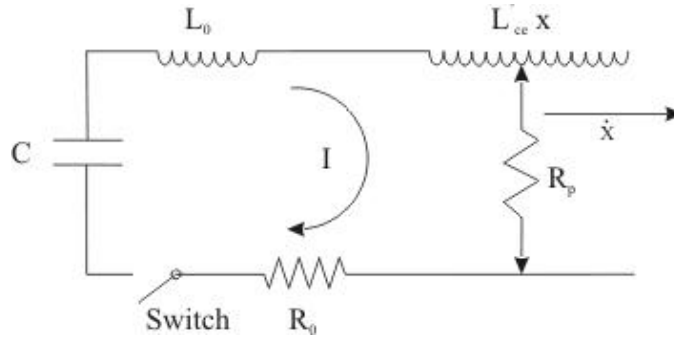


**Figure 1.7  PPT electric circuit diagram.**

Kirchhov's voltage law applied across this circuit yields the circuit equation,

$$V_0 - \frac{1}{C}\int_0^t I(\tau)d\tau + \frac{d}{dt}\left[\left(L_0 + L_{ce}'x_s\right)I\right] + \left(R_0 + R_p\right)I = 0, \qquad (2.13)$$

with $L_{ce}'$ being the inductance per unit coaxial electrode length, given by

14

$$L_{ce}^{'} = 2\ln\left(\frac{r_o}{r_i}\right),$$
(2.14)

where $r_o$ and $r_i$ are, respectively, the outer and inner electrode radii.

For the dynamical system, the current sheet was modeled as an initial mass, $m_0$, being accelerated electromagnetically down the channel gap with a distribution of gas throughout the channel. The snowplow model diverges from the slug model at this point with initial current sheet mass "sweeping up" this downstream mass as it accelerates down the channel. This current sheet effectively acts as a piston as it travels out of the thruster.

Just as in the previous parallel plate models, the two systems (electrical and dynamical) were connected by equating the change in momentum of the current sheet to the impulse acting on it. The force acting on the current sheet "piston" due to the Lorentz force acting on it was modeled as before

$$F_L = \frac{1}{2}L_{ce}^{'}I^2.$$
(2.15)

Thus, Newton's second law of motion for the system is,

$$\frac{d}{dt}\left(m\dot{x}_s\right) = \frac{1}{2}L_{ce}^{'}I^2$$
(2.16)

where $m = \left(m_0 + m^{'}x_s\right)$ and $m^{'}$ was the mass per unit channel length.

Michels et al. (1966) developed a highly modified version of Hart's snowplow model. One major adaptation allowed for a variable initial mass-loading distribution. This allowed for a gas distribution over the range between constant mass distributions

over the channel $(\alpha = 1)$ to the slug model case with all mass located at the back of the thruster channel $(\alpha = 0)$

$$m = m_0 \left[ 1 - \left( 1 - \frac{x_s}{l} \right)^{\frac{1}{1-\alpha}} \right], \qquad (2.17).$$

where $\alpha$ and $l$ are, respectively, the mass loading parameter and the channel length. Additionally, this model incorporated the effect of wall drag, ionization, and radiation losses through an additional variable, the plasma temperature, $T$. With three unknowns, this model is described by a coupled, three integro-differential equation system. These three equations are the circuit equation (Kirchhoff's Law), the momentum equation, and the plasma energy equation. The circuit equation for the system was derived by differentiating the circuit-energy equation and dividing by $I$,

$$\frac{1}{C} \int_0^t I(\tau) d\tau = \frac{d}{dt} \left\{ \left[ L_0 + L_{ce}' x_s(t) \right] I(t) \right\} + RI(t) +$$

$$\frac{1}{I(t)} \left[ 1 - P(T) \right] \left\{ \Phi_1 \left[ \frac{d}{dt} \left[ \frac{m(t)}{m_i} \right] + \Gamma(T) \right] + \left[ \frac{m(t)}{m_i} \right] \Phi_2 \right\}. \qquad (2.18)$$

The terms $\Gamma$, $\Phi_1$, $\Phi_2$, $m_i$ and $P$ appearing in this equation are, respectively, the particle diffusion current, ionization-excitation potential per ion, the excitation loss rate parameter, the average ion mass and the fraction of ionization and excitation accomplished at the expense of the plasma thermal energy. This circuit equation includes terms for electrical energy lost by radiation and absorbed in both ionizing and exciting particles swept up by the current sheet and in re-ionizing and re-exciting particles that have diffused to the walls. The momentum equation had only one extra

16

term, which removes the forward momentum of every particle which strikes the wall. Therefore, the equation of motion was given as

$$\frac{d}{dt}\left[m\dot{x}_s(t)\right] = \frac{1}{2}L_{ce}'\left[I(t)\right]^2 - m_i\Gamma(T)\dot{x}_s(t). \tag{2.19}$$

The plasma energy equation is the most significant addition to the simple snowplow model. It includes two heating sources, ohmic heating and the rate of heating due to thermalization of kinetic energy. On the other hand, the equation includes four energy loss terms. These are the losses associated with particle diffusion, ionization and excitation losses, losses due to conduction of heat energy in the electron gas and convective losses associated with the main electron conduction current. Accordingly, the plasma energy equation is as follows,

$$\frac{d}{dt}\left[\frac{3}{2}kT(1+z)\frac{m(t)}{m_i}\right] = R_p\left[I(t)\right]^2 + \frac{1}{2}\dot{m}\left[\dot{x}_s(t)\right]^2 - \frac{3}{2}kT(1+z)\Gamma(T)\left[\dot{x}_s(t)\right]^2 -$$
$$P(T)\left\{\Phi_1\left[\frac{\dot{m}(t)}{m_i}+\Gamma(T)\right]+\frac{m(t)}{m_i}\Phi_2\right\} - \int_{wall}\left(-K\nabla T\right)dS - \frac{3}{2}kT\left(\frac{|I|}{e}\right), \tag{2.20}$$

where $K$, $z$ and $e$ are, respectively, the thermal conductivity of the electron gas, the average ion charge and the charge of an electron. Michels' model is by far the most advanced snowplow model published, in that it attempts to model many of the physical phenomena that are occurring in the GFPPT. Models appearing after Michels' model are all the simple snowplow type like Hart's. The only noteworthy exception to this was in Ziemer and Choueiri's [1998] coaxial GFPPT model. In this model the mass distribution equation is derived from a one-dimensional kinetic theory description of a gas column expanding out into a vacuum.

$$m(t) = m_0 + \int_0^{x_s(t)} m' e^{-\frac{x^{*2}}{b^2}} dx^*$$  (2.21)

## 1.3.    Review of Applied Magnetic Field PPT

The first applied magnetic field study was performed by a group at the University of Tokyo (UOT) during the years of 1976-1984.  Over the course of these eight years, three publications were released detailing the experimental investigations of a number of thruster and applied field configurations (Table 2.1)

**Table 1.1  UOT Applied Magnetic Field PPT Experimental Data**

| Publication Year | 1978 | | 1979 | | 1984 |
|---|---|---|---|---|---|
| Geometry | Coaxial | Parallel Plate | Parallel Plate Straight | Parallel Plate Flared | Parallel Plate Straight |
| Inner Radius (cm) | 0.4 | - | - | - | - |
| Outer Radius (cm) | 2.0 | - | - | - | - |
| Gap Width (cm) | - | 1.8 | 4.0 | 4.0-6.0 | 4.0      5.0 |
| Plate Width (cm) | - | 1.2 | 1.2 | 1.2-4.0 | 1.2 |
| Channel Length (cm) | 1.0 | 5.5 | 5.5 | 5.5 | 6.0 |
| Initial Voltage (V) | 1350-2300 | 1000-1500 | 2500 | 2500 | 2500 |
| Capacitance (µF) | 400 | 5.1 | 4.7      10 | 4.7      10 | 40 |
| Initial Inductance (nH) | 1500 | -- | 65      250 | 65      250 | 120 |
| Mass Bit (µg) | 130-530 | 6-18 | 10-55 | 5-55 | 60-320 |
| External Field Type | Axial Diverging | Accelerating | Accelerating/ Retarding | Accelerating/ Retarding | Accelerating |
| Field Mechanism | Electro | Electro | Electro/ Permanent | Electro/ Permanent | Permanent |

In the preliminary experiments, electromagnets were applied to both coaxial and parallel plate thruster geometries [Kimura et al., 1978].  In the case of the coaxial geometry the applied magnetic field was axially diverging applied by a pulse-forming network connected to a coil of wire wound around the outside of the outer electrode. Two variations of this geometry were tested, one with the cathode as the inner electrode and the other with the cathode as the outer electrode.  While the results for both coaxial variations showed improvements over nominal operation, with up to a 50% increase in impulse bit with a 0.5 T external field, the parallel plate experiments showed significantly

better results. In the parallel plate case, the external magnetic field was applied orthogonal to the current sheet in a direction that would produce an accelerating Lorentz force for the first half wavelength of the capacitor discharge. This accelerating field was applied by two magnetic coils, one on each side of the thruster channel, connected to a pulse forming network. The results for impulse bit showed a 100% increase over the nominal value, at an applied magnetic of only 0.2 T.

With this encouraging parallel plate result, the group shifted their applied magnetic field investigation toward this geometry. In their next published work, both electromagnets and permanent magnets were utilized in producing accelerating and retarding external magnetic fields in parallel plate PPTs [Kimura, 1979]. The results for this extensive investigation were slightly different than the preliminary investigation. For the case of an accelerating external magnetic field, the impulse bit was found to initially drop with an increase in applied magnetic field and then slowly increase thereafter. The opposite was found to be the case for a retarding external magnetic field. For these fields, there is an initial increase in impulse bit with magnetic field, then a slight decrease thereafter. This result, when taken with the mass bit data, indicated that an applied magnetic field could be used to change the thruster acceleration mechanism. A retarding magnetic field was found to cause the thruster to operate predominately gas dynamically, while an accelerating field causes the electromagnetic Lorentz force to predominate. The specific impulse data for each applied field confirms this conclusion. For a retarding field the specific impulse decreases with field strength with the opposite happening for an accelerating magnetic field. In the case of the accelerating external field, at a field strength of 0.35 T, the specific impulse increased at a rate as high as 2500 s per Tesla, the

thrust efficiency increased around 15 % per Tesla.  The maximum decrease in impulse bit for an accelerating field was around 30% and occurred at 0.1 T.

In their last work with accelerating magnetic fields, the Japanese group examined the effects of accelerating magnetic fields in a single parallel plate geometry [Takegahara et al., 1984].  Additionally, in this work, it appears that the mechanism for magnetic field application was permanent magnets.  The improvements in this case, were similar in magnitude to the previous experiments, with an increase in specific impulse at a rate of and 9000 s per Tesla and an increase in thrust efficiency of 30% per Tesla.  The impulse bit, in this case, exhibited a much more significant drop around 50% of its nominal value at a field strength of 0.3 T.

After their 1984 work, the UOT group, for reasons unknown, abandoned their pursuit of applied magnetic field PPTs and for 18 years the idea lay relatively dormant. Only recently, in work here at WPI, have applied magnetic field PPTs been reexamined [Gatsonis et al, 2004].  This modeling work addresses applied magnetic field PPTs from a control engineering perspective by utilizing the fields as an actuator in the PPT system. A closed-loop feedback controller was designed and simulated through an electromechanical slug model.  The feedback controller simulations presented in this paper were shown to increase performance of the PPT through an increase in exhaust velocity over the case of no control.

## 1.4.    Objectives and Approach

With the recent interests in PPTs, research and investigations throughout industry and academia have been numerous.  Much of this effort has been conducted to optimize thruster performance through a better understanding of the fundamental plasma dynamics

in the plume and electrode regions of the thruster. Despite this increase in research, the prospect of using flow control engineering for PPT optimization has not been recently addressed. This lack of control engineering is also the case for most other electric propulsion devices. Flow control involves taking a flow system that has a set of inputs and outputs (e.g. voltage, velocity, current, etc.) and manipulating the inputs to realize a specific desired output. This type of control could be utilized to optimize such PPT system performance parameters as the specific impulse and impulse bit using inputs such as an external magnetic field.

This thesis is aimed at exploring the possibility of using flow-control for PPT performance optimization. The introduction presents the PPT with its various types and geometric configurations and discusses its accompanying history.

Objectives and Approach:

- Develop an improved electromechanical model for the parallel-plate PPT.

- Develop a software package modeling a general PPT with a graphical user interface (GUI) to simulate various PPT types, geometric configurations, and parameters.

- Develop an electromechanical model modified to include externally applied magnetic field effects.

- Using this modified model, examine the effects of externally applied magnetic fields on PPT performance.

- Propose and design an open-loop controller to optimize the specific impulse and thrust efficiency of a PPT.

The choice of one dimensional PPT plasma flow models is critical in this control study and so a review of previously published models appearing over the last 40 years is

presented in chapter two. This chapter also details the equally important externally applied magnetic field work performed at the University of Tokyo (UOT). Chapter three presents the general one-dimensional PPT model and the modified version of this model that includes applied magnetic field effects. Chapter four discusses the numerical scheme employed in solving this model and details the GUI implemented for the general model. Additionally, both the general and modified models are validated in this chapter. Chapter five presents the control strategy and controller that were utilized in this study and presents a brief control analysis of the modified model system. Chapter six presents the simulation of the controller in various PPTs determining its effects on thruster performance. Chapter seven presents the overall conclusions, addressing the results and contributions of this work, and gives recommendations for future research.

# Chapter 2

# An Improved Electromechanical PPT Model

## 2.1. Introduction

A low-order dynamical model is used to describe the current sheet motion in rectangular and coaxial PPT geometries. Slug and snowplow models were chosen to accomplish this due to their simplicity and proven accuracy. Furthermore, their simplicity warrant use as tools for developing a control strategy for PPT operation. This strategy was implemented and investigated by the use of a version of these models modified to include externally applied magnetic field effects.

The basis of the one dimensional PPT model is to approximate the PPT system as an electromechanical device with an electrical circuit interacting with a dynamical system. The electric circuit is theoretically idealized in both models as a LCR circuit with discrete, albeit moveable, elements. The physical law which is used to describe the dynamics of the circuit is Kirchoff's voltage law, which is itself derived from Maxwell's charge continuity equation for the circuit. In general, the inductance and current are functions of time with all other parameters, including resistance, remaining constant over the acceleration process. The dynamical system is idealized as an initial mass of plasma being accelerated by a Lorentz $\mathbf{j} \times \mathbf{B}$ force out of the thruster. Accordingly, the physical

law used to describe the situation is Newton's second law of motion. The difference between the slug and snowplow variations of the model is in the mass of the current sheet. In the slug model, the initial mass is constant throughout the entire process. On the other hand, in the snowplow model, the initial mass of plasma entrains additional ambient gas mass as it propagates out of the thruster.

This chapter includes the derivations of both the general models for parallel plate and coaxial PPT geometries as well as a modified model for the parallel plate geometry. The derivation includes details of the self-induced magnetic field, the inductance model, the plasma resistance model and the mass distribution model utilized for each geometry. Beside the electrode geometry, PPTs are further classified as either ablative or gas-fed based on the propellant utilized (Figure 2.1).
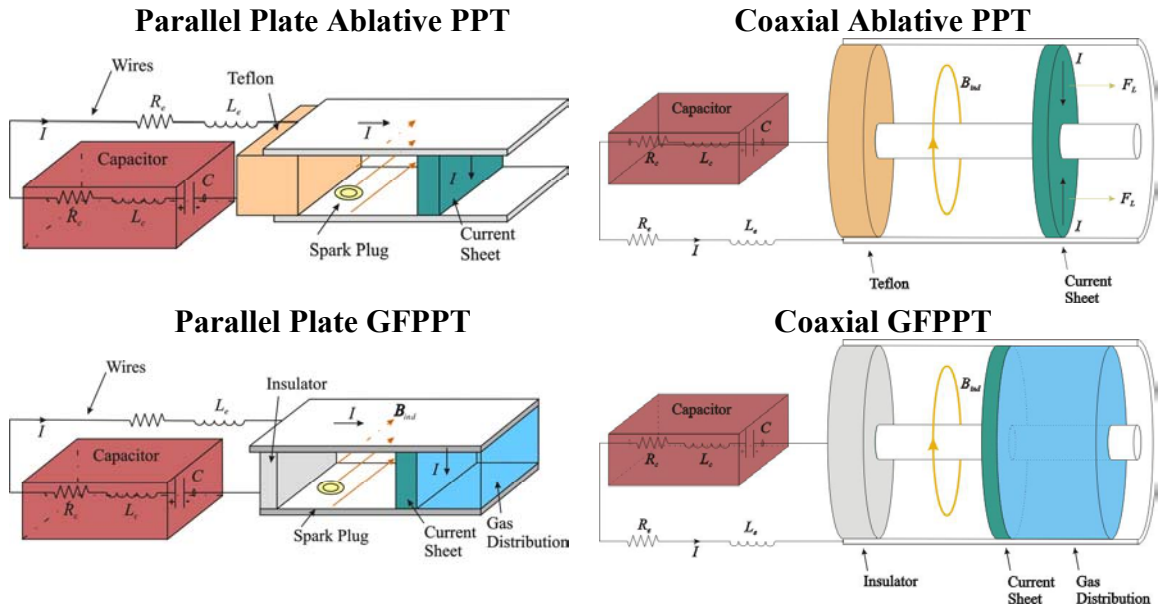


**Figure 2.1  PPT Types**

Variations of the electromechanical model specifically addressing these operating regimes are presented for each geometry. Though not commonly investigated, the parallel-plate GFPPT was modeled in this study, due in part to the recent experiments of

Ziemer et al. (1999 and 2000) examining these thrusters from an experimental perspective. Generally, ablative PPTs have a constant mass bit equal to the initial mass, $m_0$, however, for side-fed ablative thrusters, the current sheet mass will increase as it traverses down the channel, $m_t \neq 0$. This configuration can be simulated through applying the snowplow model.

## 2.2.    Generalized Electromechanical Model for a Parallel-Plate PPT
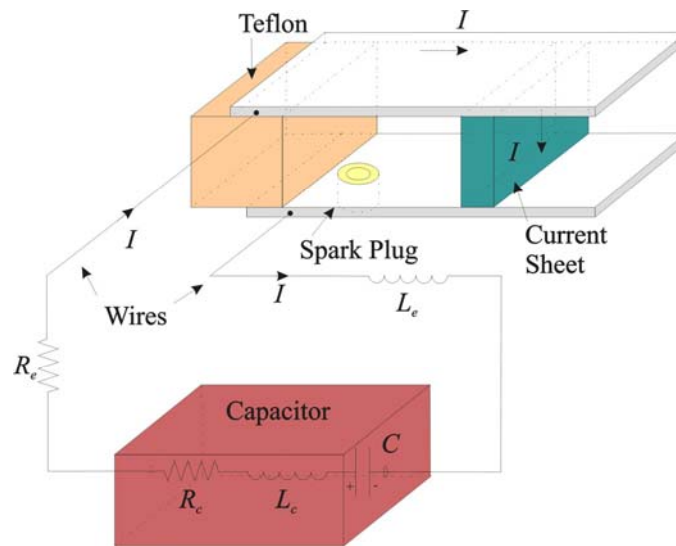


**Figure 2.2  Parallel plate APPT.**

The parallel plate PPT thruster, shown in Figure 2.2, with the moving discharge, is described electrically as an LCR circuit as in Figure 2.3.
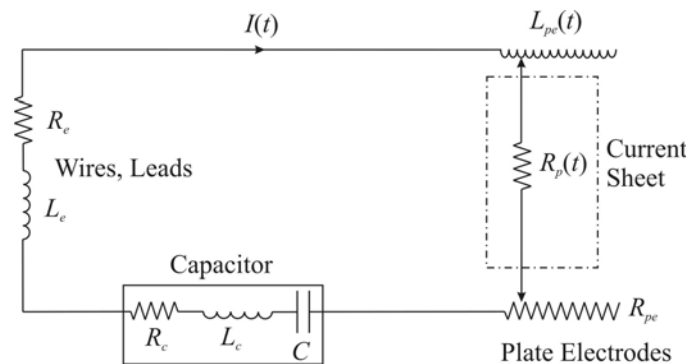


**Figure 2.3  Circuit model for parallel plate PPT.**

The inductance terms $L_c$, $L_{pe}$ and $L_e$ are due, respectively, to the capacitor, the plate electrode geometry and the wires and leads. The resistance terms $R_c$, $R_e$, $R_{pe}$ and $R_p$ are due, respectively, to the capacitor, the wires and leads, the plate electrodes and the plasma. Applying Faraday's law around the circuit depicted in Figure 3.2 yields

$$V_C(t) = IR_T(t) + \frac{d}{dt}\left[\lambda_{PPT}(t)\right],\tag{2.1}$$

where $R_T(t) = R_c + R_e + R_{pe} + R_p(t)$ and $\lambda_{PPT}(t)$ is the total flux linkage through the PPT circuit. The flux linkage can be written in terms of the components of the PPT as

$$\lambda_{PPT}(t) = \lambda_c(t) + \lambda_e(t) + \lambda_{pe}(t),\tag{2.2}$$

where the three terms on the right are, respectively, the magnetic flux due to the capacitor inductance, the wire and lead inductance and the flux through the plate electrode channel. Rewriting (2.2) in terms of the capacitor and wire and lead self-inductances yields

$$\lambda_{PPT}(t) = L_c I(t) + L_e I(t) + \iint\limits_{electrodes} \mathbf{B}_{ind}(x,y) \cdot d\mathbf{A},\tag{2.3}$$

where $L_c$, $L_e$, $\mathbf{B}_{ind}$ and $\mathbf{A}$ are, respectively, the capacitor self-inductance, the wire and lead self-inductance, the self-induced field throughout the current sheet and an area vector.

### 2.2.1. Parallel-Plate Self-Induced Magnetic Field

The magnetic field behind the current sheet is found by first assuming the parallel-plate geometry can be approximated as quasi-infinite width, one-turn solenoid composed of perfectly conducting sheets (Figure 2.4).

26
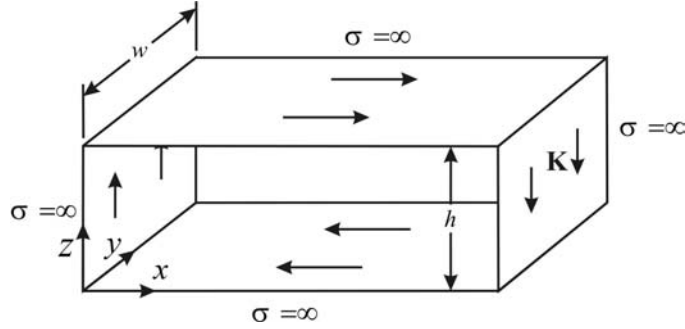
**Figure 2.4  Perfectly conducting one-turn solenoid**

Other than perfect conduction, this approximation also assumes that that each sheet has a uniform current per unit width, $K$ and that $w \gg h$. These simplifications contrast with a real parallel-plate PPT in the following ways.  First, though the electrodes will have a very high conductivity, which can be quite accurately approximated as infinite, the plasma current sheet will have a finite conductivity.   This finite plasma conductivity will also lend to the current sheet having a thickness, $\delta$, in contrast to the sheet assumption. Finally, most parallel plate geometries have that $h > w$, and are expected to exhibit fringe effects in contrast to the one-turn solenoid approximation.

The magnetic field contained within the one-turn solenoid will satisfy Ampere's continuity condition with the following boundary conditions on the perfect conductor [Haus et al., 1989, pp 335]

$$\mathbf{n} \cdot \frac{\mathbf{B}_{ind}}{\mu_0} = 0, \tag{2.4}$$

$$\mathbf{n} \times \frac{\mathbf{B}_{ind}}{\mu_0} = \mathbf{K}, \tag{2.5}$$

where $\mathbf{n}$ is the normal area vector and $\mathbf{K}$ is the current per unit width vector.   This gives the magnetic field inside of the quasi-infinite width, one turn solenoid as

$$\mathbf{B}_{ind} = \mu_0 K \hat{\mathbf{y}} = \mu_0 \frac{I}{w} \hat{\mathbf{y}} \qquad (2.6)$$

The magnetic field throughout the current sheet can be found by applying Ampere's Law to a surface $S$ passing through the current sheet and using the magnetic field inside the solenoid (2.6) as a boundary condition (Figure 2.5).
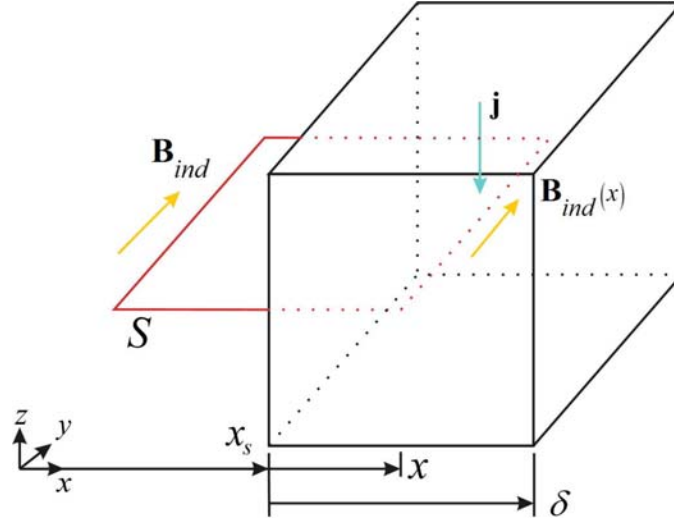


**Figure 2.5  Ampere's Law applied throughout the current sheet**

If the current density throughout the sheet is uniform and equal to

$$\mathbf{j}(t) = -\frac{I(t)}{w\delta} \hat{\mathbf{z}}, \qquad (2.7)$$

then the magnetic field throughout the sheet will be given by,

$$\mathbf{B}_{ind}(x,t) = \mu_0 \frac{I(t)}{w} \left[ 1 - \frac{x - x_s(t)}{\delta} \right] \hat{\mathbf{y}}. \qquad (2.8)$$

The magnetic field in front of the current sheet can be found similarly and is equal to zero. Therefore, taking (2.6) and (2.8) together with zero field ahead of the current sheet gives the full description of the magnetic field used in this model

28

$$\mathbf{B}_{ind}\left(x,t\right) = \begin{cases} \mu_0 \dfrac{I\left(t\right)}{w}\hat{\mathbf{y}}, & 0 < x < x_s\left(t\right) \\[3mm] \mu_0 \dfrac{I\left(t\right)}{w}\left[1-\dfrac{x-x_s\left(t\right)}{\delta}\right]\hat{\mathbf{y}}, & x_s\left(t\right) < x < x_s\left(t\right)+\delta. \\[3mm] 0, & x > x_s\left(t\right)+\delta \end{cases} \tag{2.9}$$

### 2.2.2. Parallel-Plate Inductance Model

Going back the equation (2.3) and substituting the plate electrode magnetic field (2.9) yields

$$\lambda_{PPT}\left(t\right) = L_c I\left(t\right) + L_e I\left(t\right) + \int_0^{x_s(t)}\int_0^h \mu_0 \frac{I\left(t\right)}{w}dydx + \int_{x_s(t)}^{x_s(t)+\delta}\int_0^h \mu_0 \frac{I\left(t\right)}{w}\left[1-\frac{x-x_s\left(t\right)}{\delta}\right]dydx. \tag{2.10}$$

Integrating the later two terms yields

$$\lambda_{PPT}\left(t\right) = L_c I\left(t\right) + L_e I\left(t\right) + \left[\mu_0 \frac{h}{w}x_s\left(t\right) + \mu_0 \frac{\delta}{2}\frac{h}{w}\right]I\left(t\right). \tag{2.11}$$

The term in brackets in equation (2.11) is the self-inductance due to parallel-plate electrodes,

$$L_{pe}\left(x_s\left(t\right)\right) = \frac{\lambda_{pe}\left(x_s\left(t\right)\right)}{I\left(t\right)} = \mu_0 \frac{h}{w}x_s\left(t\right) + \mu_0 \frac{\delta}{2}\frac{h}{w} \tag{2.12}$$

For an infinitesimally thin current sheet, $\delta = 0$, the model reduces to

$$L_{pe}\left(x_s\left(t\right)\right) = \mu_0 \frac{h}{w}x_s\left(t\right) \tag{2.13}$$

Equation (2.13) is the same plate electrode inductance term appearing in Jahn's [1968] pulsed accelerator model.

The motion of the current sheet is described dynamically by Newton's second law,

29

$$\frac{d}{dt}\left[m(t)\dot{\mathbf{x}}_s(t)\right] = \sum \mathbf{F}(t), \tag{2.14}$$

where $m(t)$ is the mass of the current sheet and $\sum \mathbf{F}(t)$ is the sum of the forces acting on it. In the generalized model, mass being accelerated is modeled as unsteady throughout the process. Assuming the force acting on the current sheet is a $\mathbf{j} \times \mathbf{B}$ Lorentz force, $\mathbf{F}_L(t)$, gives

$$\frac{d}{dt}\left[m(t)\dot{\mathbf{x}}_s(t)\right] = \mathbf{F}_L(t) = \iiint_{\substack{current \\ sheet}} \mathbf{j} \times \mathbf{B} dV. \tag{2.15}$$

Substituting (2.7) and (2.9) into (2.15) yields

$$\mathbf{F}_L(t) = \iiint_{\substack{current \\ sheet}} \mu_0 \frac{[I(t)]^2}{\delta w^2} \hat{\mathbf{x}} \left[1 - \frac{x - x_s(t)}{\delta}\right] dxdydz =$$

$$\mu_0 \frac{h[I(t)]^2}{w\delta} \hat{\mathbf{x}} \int_{x_s(t)}^{x_s(t)+\delta} \left[1 - \frac{x - x_s(t)}{\delta}\right] dx = \frac{1}{2}\mu_0 \frac{h}{w}[I(t)]^2 \hat{\mathbf{x}}. \tag{2.16}$$

Substituting this into (2.15) gives the dynamic equation for the electromechanical model

$$\frac{d}{dt}\left[m(t)\dot{\mathbf{x}}_s(t)\right] = \frac{1}{2}\mu_0 \frac{h}{w}[I(t)]^2 \hat{\mathbf{x}}. \tag{2.17}$$

### 2.2.3. Mass Distribution Model

The mass of the current sheet was modeled as in Michels et al [1966]

$$m(t) = m_0 + m_t \left[1 - \left(1 - \frac{x_s(t)}{l}\right)^{\frac{1}{1-\alpha}}\right], \tag{2.18}$$

where $\alpha$ is the mass distribution loading parameter, $m_0$ is the initial current sheet mass and $m_t$ is the additional mass entrained or taken up into the current sheet. This mass function was chosen as it allowed for mass distributions ranging from a uniform

distribution down the channel at $\alpha = 0$ to a slug mass at an $\alpha = 1$ (all mass contained within the current sheet at $t = 0$). Figure 2.6 shows the mass of the current sheet as a function of the distance traversed down the channel for various $\alpha$.
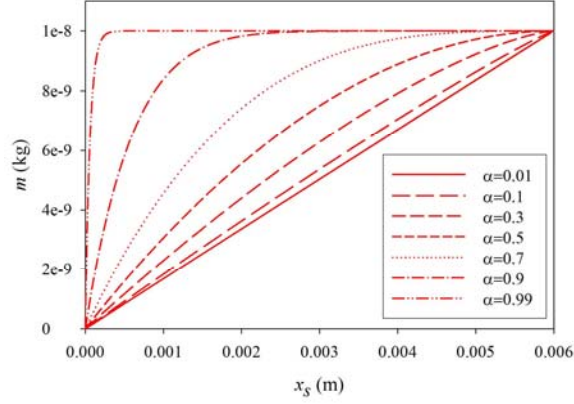


**Figure 2.6  Mass distribution function.**

Utilizing this mass function the dynamic equation becomes

$$m(t)\ddot{x}_s(t) + \dot{m}(t)\dot{x}_s(t) = \frac{1}{2}\mu_0 \frac{h}{w}\left[I(t)\right]^2,$$

(2.19)

with $m(t)$ given by (2.18) and

$$\dot{m}(t) = \frac{m_t \dot{x}_s(t)}{l(1-\alpha)}\left[1 - \frac{x_s(t)}{l}\right]^{\frac{\alpha}{1-\alpha}}.$$

(2.20)

## 2.2.4.  Parallel-Plate Plasma Resistance Model

At this point nothing has been said about the plasma resistance, $R_p(t)$ appearing in the circuit equation (2.1). Ziemer et al. [2001] notes the importance this parameter has on overall PPT performance and earlier noted the idea of using "... a more realistic model of the plasma conductivity..." [1997] in a one dimensional PPT model. Previous one dimensional models have utilized a constant value of resistance that was either experimentally measured or that which yielded a best-fit with current and voltage

waveform experimental data [Leiweke, 1996]. As a means to increase the model's predictive capabilities, it was desirous to develop a plasma resistance model relying as much as possible on first principles.

To incorporate a plasma resistance model, the plasma conductivity was approximated by the Spitzer-Harm model assuming that the plasma is fully ionized and singly charged [Mitchner et al., 1973]. The plasma resistance is then,

$$R_p(t) = \frac{l}{\sigma A} = \frac{h}{\sigma_p w \delta},$$
(2.21)

where, $\sigma_p$ is the plasma conductivity and $\delta$ is the current sheet thickness. Since, the diffusion of the self-magnetic field into the current sheet plasma will be governed by the diffusion equation, the current sheet thickness can be estimated as the magnetic diffusion depth (skin depth) [Haus et al., 1989];

$$\delta = \sqrt{\frac{\tau}{\sigma_p \mu_0}},$$
(2.22)

where $\tau$ is a characteristic pulse time equal to a quarter of the PPT ringing period. The Spitzer conductivity is given as [Mitchner et al., 1973];

$$\sigma_p = 1.53 \times 10^{-2} \frac{T_e^{\frac{3}{2}}}{\ln \Lambda},$$
(2.23)

where, $\Lambda$ is the ratio of the Debye length and the impact parameter,

$$\Lambda = \frac{\lambda_D}{b_0} = 1.24 \times 10^7 \left( \frac{T_e^3}{n_e} \right)^{\frac{1}{2}}.$$
(2.24)

Taking equations (2.21),(2.22), (2.23) and (2.24) together yields the plasma resistance model utilized throughout this work

$$R_p = 8.08 \frac{h}{T_e^{\frac{3}{4}} w} \sqrt{\frac{\mu_0 \ln\left[1.24 \times 10^7 \left(\frac{T_e^3}{n_e}\right)^{\frac{1}{2}}\right]}{\tau}} \qquad (2.25)$$

The plasma resistance is mainly a function of the plasma temperature. Therefore, applying an appropriate function for plasma temperature with time, would specify the plasma resistance throughout the discharge. In this thesis, a constant value of plasma temperature was utilized based on average plasma temperature measurements of similar power level thrusters. Figures 2.7 and 2.8 display the plasma resistance versus plasma temperature for the LES-6 and the LES-8/9 PPT for various electron number densities using equation (2.25).
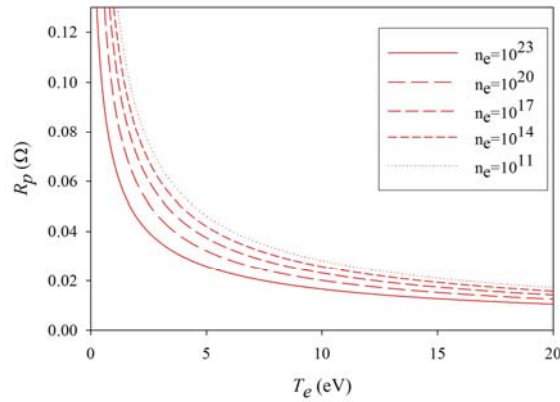


**Figure 2.7  Plasma resistance model for LES-6 PPT.**
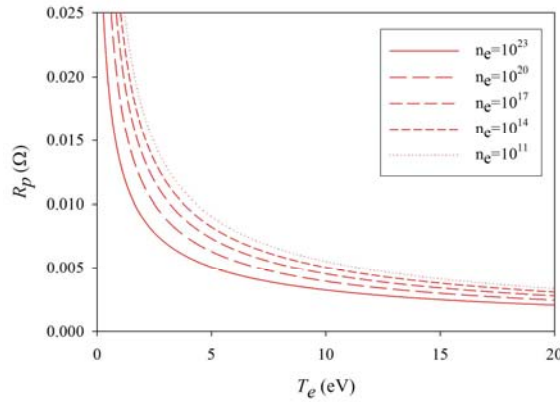


**Figure 2.8  Plasma resistance model for LES-8/9 PPT.**

### 2.2.5. Summary of the Parallel-Plate Electromechanical Model

To wrap up this model derivation, the initial conditions of this system of two, second order ODE's must be specified. These are given as

$$x_s(0) = 0, \ \dot{x}_s(0) = 0, \ \int_0^{t=0} I(t)\,dt = 0, \ I(0) = 0. \tag{2.26}$$

Taking the dynamic (2.17) and circuit (2.1) equations together with the initial conditions (2.26) and substituting the mass distribution function (2.18) and the plasma resistance model (2.25) constitute the generalized, one dimensional, parallel plate PPT model for unsteady plasma acceleration,

$$V_0 - \frac{1}{C}\int_0^t I(t)\,dt = I(t)\left(R_c + R_e + R_{pe} + R_p\right) +$$

$$\left[L_c + L_e + \mu_0 \frac{h}{w}x_s(t) + \mu_0 \frac{\delta}{2}\frac{h}{w}\right]\dot{I}(t) + \mu_0 \frac{h}{w}\dot{x}_s(t)I(t), \tag{2.27}$$

$$\frac{d}{dt}\left[m\dot{x}_s(t)\right] = \frac{1}{2}\mu_0 \frac{h}{w}\left[I(t)\right]^2, \tag{2.17}$$

$$m(t) = m_0 + m_t\left[1 - \left[1 - \frac{x_s(t)}{l}\right]^{\frac{1}{1-\alpha}}\right], \tag{2.18}$$

$$R_p = 8.08\frac{h}{T_e^{\frac{3}{4}}w}\sqrt{\frac{\mu_0 \ln\left[1.24\times10^7\left(\frac{T_e^3}{n_e}\right)^{\frac{1}{2}}\right]}{\tau}} \tag{2.25}$$

$$x_s(0) = 0, \ \dot{x}_s(0) = 0, \ \int_0^{t=0} I(t)\,dt = 0, \ I(0) = 0. \tag{2.26}$$

This system can be solved for $x_s(t)$ and $I(t)$ to and all other pertinent information, e.g. velocity and voltage can be derived from this solution.

The energy equation for the circuit is of particular interest in this performance optimization study. It can be derived from the circuit equation (2.27) by multiplying it by $I(t)$ and integrating over time,

$$\int_0^t I(t)V_c dt = \int_0^t \frac{d}{dt}\left\{\frac{1}{2}\left[I(t)\right]^2 L_T(t)\right\}dt + \int_0^t R_T(t)\left[I(t)\right]^2 dt + \int_0^t \frac{1}{2}\left[I(t)\right]^2 \dot{L}_T(t)dt. \quad (2.28)$$

The term to the left equal sign may be evaluated by substituting for current,

$$I(t) = -C\frac{dV_c(t)}{dt} \quad (2.29)$$

This results in the energy equation for the PPT system.

$$\frac{1}{2}CV_0^2 - \frac{1}{2}C\left[V_c(t)\right]^2 = \frac{1}{2}\left[I(t)\right]^2 L_T(t) + \int_0^t R_T(\tau)\left[I(\tau)\right]^2 dt + \int_0^t \frac{1}{2}\frac{h}{w}\mu_0\left[I(\tau)\right]^2 \dot{x}_s(\tau)dt. \quad (2.30)$$

The first term on the left hand side represents the total energy stored in the capacitor at $t = 0$. The second term on the left hand side is the time varying energy stored in the capacitor. The terms on the right are, respectively, the energy stored in the magnetic field, the energy dissipated by Ohmic heating and the work done to accelerate the current sheet mass.

## a) Slug Operation

The generalized parallel plate PPT electromechanical model can be easily adapted to the various operational modes of parallel plate PPTs. For example, in ablative PPTs the propellant mass enters the current sheet very early in the acceleration process and is accelerated electromagnetically together as one unit or "shot". This model has been come to be known as the one dimensional slug model of PPT operation. The GFPPT can

also be simulated by the slug model if the capacitor is discharged before the propellant gas has been given enough time to expand away from the back of the GFPPT channel.

Mathematically, the generalized parallel plate PPT model can be easily transformed into the slug model with a mass loading parameter $\alpha = 1$. In this model, all the propellant gas is assumed to be located all along the insulator face at $t = 0$. In the limit that $\alpha = 1$, there is no mass accumulation $(\dot{m}(t) = 0)$ as the current sheet travels down the channel as a constant mass slug with $, m(t) = m_0$. Thus, the system of equations with its accompanying initial conditions can be written as

$$V_0 - \frac{1}{C}\int_0^t I(t)\,dt =$$

$$I(t)\left(R_c + R_e + R_{pe} + R_p\right) + \left[L_c + L_e + \mu_0 \frac{h}{w}x_s(t) + \mu_0 \frac{\delta}{2}\frac{h}{w}\right]\dot{I}(t) + \mu_0\frac{h}{w}\dot{x}_s(t)I(t), (2.27)$$

$$m_0\ddot{x}_s(t) = \frac{1}{2}\mu_0\frac{h}{w}\left[I(t)\right]^2, \tag{2.31}$$

$$R_p = 8.08\frac{h}{T_e^{\frac{3}{4}}w}\sqrt{\frac{\mu_0 \ln\left[1.24\times10^7\left(\frac{T_e^3}{n_e}\right)^{\frac{1}{2}}\right]}{\tau}} \tag{2.25}$$

$$x_s(0) = 0,\ \dot{x}_s(0) = 0,\ \int_0^{t=0} I(t)\,dt = 0,\ I(0) = 0. \tag{2.26}$$

Here, it can be seen that the only changes from the general one dimensional parallel plate PPT model lie within Newton's second law equation for the system (2.31).

### b) Snowplow Operation

To model the majority of operational modes of GFPPTs, a variable current sheet mass must be assumed. In the snowplow mode, the current sheet starts off with an initially ionized mass or zero mass. This accelerating sheet sweeps up the mass it encounters as it travels down the channel. Most snowplow models assume a constant mass distribution throughout the channel ahead of the current sheet. This situation can be modeled using a mass loading parameter equal to zero. Thus, the system of equations with accompanying initial conditions becomes

$$V_0 - \frac{1}{C}\int_0^t I(t)\, dt =$$

$$I(t)\left(R_c + R_e + R_{pe} + R_p\right) + \left[L_c + L_e + \mu_0 \frac{h}{w} x_s(t) + \mu_0 \frac{\delta}{2}\frac{h}{w}\right]\dot{I}(t) + \mu_0 \frac{h}{w}\dot{x}_s(t) I(t), \quad (2.27)$$

$$m(t)\ddot{x}_s(t) + \dot{m}(t)\dot{x}_s = \frac{1}{2}\mu_0 \frac{h}{w}\left[I(t)\right]^2, \quad (2.32)$$

$$m(t) = m_0 + m_t\left[1 - \left[1 - \frac{x_s(t)}{l}\right]^{\frac{1}{1-\alpha}}\right], \quad (2.18)$$

$$R_p = 8.08\frac{h}{T_e^{\frac{3}{4}}w}\sqrt{\frac{\mu_0 \ln\left[1.24\times10^7\left(\frac{T_e^3}{n_e}\right)^{\frac{1}{2}}\right]}{\tau}} \quad (2.25)$$

$$x_s(0) = 0,\ \dot{x}_s(0) = 0,\ \int_0^{t=0} I(t)\, dt = 0,\ I(0) = 0. \quad (2.26)$$

If a non-uniform mass distribution is to be modeled, the general model (2.27), (2.32), (2.18), (2.25) and (2.26) may be applied with a mass loading parameter between zero and one. The kinetic gas theory mass model (2.21) described by Ziemer et al. [1998] can be

37

approximated using the mass distribution model (2.18) through the correct choice of parameters $\alpha$ and $l$.

## 2.2.    Generalized Electromechanical Model for a Coaxial PPT
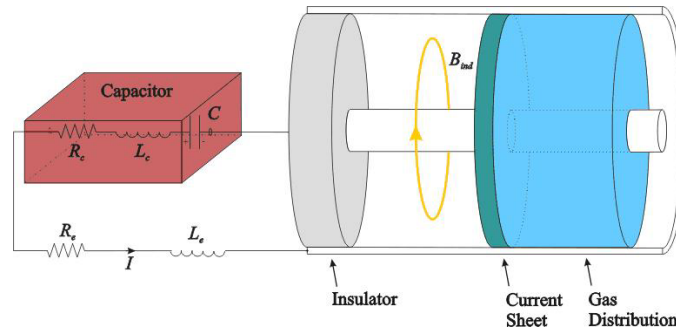


**Figure 2.9  Coaxial GFPPT.**

Due to the operational similarity of coaxial PPTs with their parallel plate counterparts, they can be modeled in the same way, as an electrical system interacting with a mechanical system.  As seen in comparing figure 2.10 with 2.3, the electrical system is identical for both the coaxial and parallel plate one dimensional models with the exception of the coaxial plate inductance term.
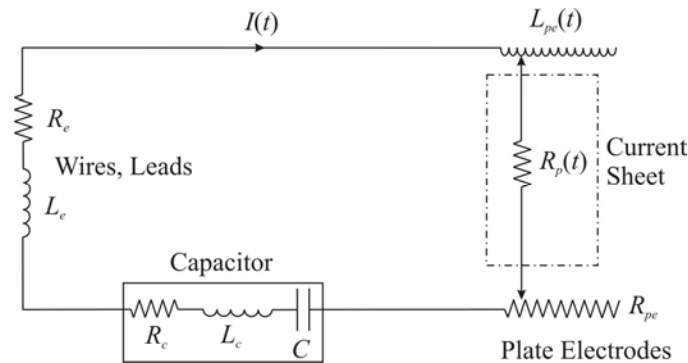


**Figure 2.10  Circuit model of a coaxial PPT.**

Accordingly, this general coaxial derivation is identical to the general parallel plate derivation for equations (2.1) through (2.3) involving the circuit equation.  Differences

arise due to the dissimilar induced magnetic fields and plasma current densities produced by the devices.

## 2.2.1. Coaxial Self-Induced Magnetic Field

The induced magnetic field behind the current sheet within this coaxial conductor can be found by applying Ampere's Law to a surface $S$ with radius $r$ and an outer contour $C$ around the inner electrode (Figure 2.11) [Haus et al., 1989].
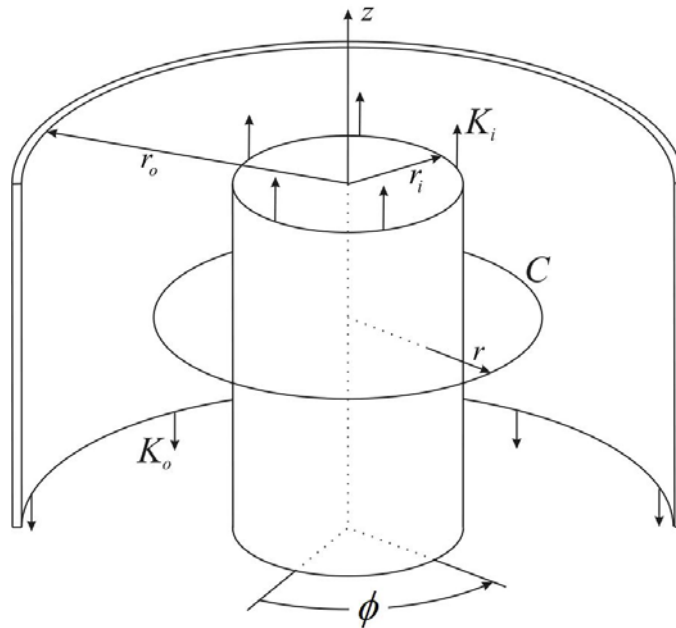


**Figure 2.11  Coaxial PPT cutaway with uniform surface current.**

The current in a coaxial conductor operated with a low characteristic pulse time will be dominated by the skin effect.  Accordingly, the current will flow nearly entirely on the outer surface of the inner electrode and on the inner surface of the outer electrode.  This gives Ampere's Law as

$$\int_0^{2\pi} \mu_0 B_\phi(t) r\,d\phi = \int_0^{2\pi} K_i(t) r_i\,d\phi, \tag{2.33}$$

39

where $B_\phi$ is the self-induced azimuthal magnetic field and $K_i(t)$ is the surface current density on the inner electrode given by

$$K_i(t) = \frac{I(t)}{2\pi r_i}.$$ (2.34)

Solving (2.33), substituting (2.34), and writing the azimuthal component as a vector field gives

$$\mathbf{B}_{ind}(t) = -\mu_0 \frac{I(t)}{2\pi r}\hat{\boldsymbol{\varphi}},$$ (2.35)

which fully describes the magnetic field in the region between the electrodes. The current sheet current density will also have a different structure than for the parallel plate geometry. Assuming the current is uniformly distributed throughout the sheet gives a current density that varies in the radial direction between the electrodes as

$$\mathbf{j}(t) = -\frac{I(t)}{2\pi\delta r}\hat{\mathbf{r}}.$$ (2.36)

The magnetic field throughout the current sheet can be found by applying Ampere's Law in a similar way as was done for the parallel plate geometry. This gives the magnetic field throughout the sheet as,

$$\mathbf{B}_{ind}(t,x,r) = -\mu_0 \frac{I(t)}{2\pi r}\left(1 - \frac{x - x_s(t)}{\delta}\right)\hat{\boldsymbol{\varphi}}.$$ (2.37)

The magnetic field in front of the current sheet can be found similarly and is equal zero as it was for the parallel plate geometry. Taking (2.35) and (2.37) together with zero field ahead of the current sheet gives the full description of the magnetic field used in this general coaxial model

40

$$\mathbf{B}_{ind}(t,x,r) = \begin{cases} -\mu_0 \dfrac{I(t)}{2\pi r}\hat{\varphi}, & 0 < x < x_s(t) \\[2ex] -\mu_0 \dfrac{I(t)}{2\pi r}\left[1 - \dfrac{x - x_s(t)}{\delta}\right]\hat{\varphi}, & x_s(t) < x < x_s(t) + \delta. \\[2ex] 0, & x > x_s(t) + \delta \end{cases} \qquad (2.38)$$

### 2.2.2. Coaxial Electrode Inductance Model

Substituting (2.38) into equation (2.3) yields

$$\lambda_{PPT}(t) = L_c I(t) + L_e I(t) +$$

$$\int_0^{x_s(t)} \int_0^{2\pi} \int_{r_i}^{r_o} \mu_0 \frac{I(t)}{2\pi r} r\varphi \, dr \, dx + \int_{x_s(t)}^{x_s(t)+\delta} \int_0^{2\pi} \int_{r_i}^{r_o} \mu_0 \frac{I(t)}{2\pi r}\left[1 - \frac{x - x_s(t)}{\delta}\right] r\varphi \, dr \, dx, \qquad (2.39)$$

which integrates to

$$\lambda_{PPT}(t) = L_c I(t) + L_e I(t) + \left[\mu_0 \frac{x_s(t)}{2\pi} \ln\left(\frac{r_o}{r_i}\right) + \mu_0 \frac{\delta}{4\pi} \ln\left(\frac{r_o}{r_i}\right)\right] I(t). \qquad (2.40)$$

This gives the coaxial electrode inductance model as

$$L_{ce}(x_s(t)) = \frac{\lambda_{ce}(x_s(t))}{I(t)} = \mu_0 \frac{x_s(t)}{2\pi} \ln\left(\frac{r_o}{r_i}\right) + \mu_0 \frac{\delta}{4\pi} \ln\left(\frac{r_o}{r_i}\right). \qquad (2.41)$$

Similar to the parallel-plate inductance model, for an infinitesimally thin current, $\delta = 0$, the model reduces to

$$L_{ce}(x_s(t)) = \frac{\lambda_{ce}(x_s(t))}{I(t)} = \mu_0 \frac{x_s(t)}{2\pi} \ln\left(\frac{r_o}{r_i}\right). \qquad (2.42)$$

This coaxial inductance model is the same as found in Hart's [1962] coaxial accelerator model.

The motion of the coaxial current sheet described dynamically by Newton's second law (2.14). The Lorentz force for this geometry will be given by

$$\mathbf{F}_L = \int\limits_{x_s}^{x_s+\delta} \int\limits_{0}^{2\pi} \int\limits_{r_i}^{r_o} \frac{I(t)}{2\pi\delta r} \mu_0 \frac{I(t)}{2\pi r}\left[1 - \frac{x - x_s(t)}{\delta}\right]\hat{\mathbf{x}} r dr d\phi dx,\tag{2.43}$$

which gives

$$\mathbf{F}_L = \mu_0 \frac{\left[I(t)\right]^2}{2\pi\delta}\hat{\mathbf{x}} \int\limits_{x_s(t)}^{x_s(t)+\delta} \int\limits_{r_i}^{r_o} \frac{1}{r}\left[1 - \frac{x - x_s(t)}{\delta}\right]dx = \frac{\mu_0}{4\pi}\ln\left(\frac{r_o}{r_i}\right)\left[I(t)\right]^2\hat{\mathbf{x}}.\tag{2.44}$$

Substituting this into (2.15) gives the dynamic equation for the electromechanical model

$$\frac{d}{dt}\left[m(t)\dot{\mathbf{x}}_s(t)\right] = \frac{\mu_0}{4\pi}\ln\left(\frac{r_o}{r_i}\right)\left[I(t)\right]^2\hat{\mathbf{x}}.\tag{2.45}$$

### 2.2.3. Coaxial Plasma Resistance Model

The only other change to the general parallel plate model appears in the plasma resistance model. With all other equations in this model remaining the same, the resistance equation, in this coaxial geometry, will be written as

$$R_p = \frac{l}{\sigma A} = \frac{r_o - r_i}{\sigma_p \delta\pi(r_o + r_i)},\tag{2.46}$$

where the area was taken at the average radius

$$A = \delta \cdot 2\pi\left(\frac{r_o + r_i}{2}\right) = \delta\pi(r_o + r_i).\tag{2.47}$$

Substituting equations (2.22)-(2.24)into (2.46) yields the coaxial plasma resistance model

$$R_p = 2.57\frac{r_o - r_i}{T_e^{\frac{3}{4}}(r_o + r_i)}\sqrt{\frac{\mu_0 \ln\left[1.24\times10^7\left(\frac{T_e^3}{n_e}\right)^{\frac{1}{2}}\right]}{\tau}}.\tag{2.48}$$

### 2.2.4. Summary of the Coaxial Electromechanical Model

Bringing the plasma resistance model (2.48) together with the circuit equation (2.27), dynamic equation (2.45), mass distribution model (2.18) and initial conditions (2.26) gives the general one dimensional coaxial PPT model

$$V_0 - \frac{1}{C} \int_0^t I(t)\,dt = I(t)\left\{ R_c + R_e + R_{pe} + R_p \right\} +$$

$$\left[ L_c + L_e + \frac{\mu_0}{4\pi} \ln\left(\frac{r_o}{r_i}\right) \right] x_s(t) + \mu_0 \frac{\delta}{4\pi} \ln\left(\frac{r_o}{r_i}\right) \dot{I}(t) + \frac{\mu_0}{4\pi} \ln\left(\frac{r_o}{r_i}\right) \dot{x}_s(t) I(t), \quad (2.49)$$

$$\frac{d}{dt}\left[ m(t) \dot{x}_s(t) \right] = \frac{\mu_0}{4\pi} \ln\left(\frac{r_o}{r_i}\right) \left[ I(t) \right]^2, \quad (2.45)$$

$$m(t) = m_0 + m_t \left[ 1 - \left[ 1 - \frac{x_s(t)}{l} \right]^{\frac{1}{1-\alpha}} \right], \quad (2.18)$$

$$R_p = 2.57 \frac{r_o - r_i}{T_e^{\frac{3}{4}}(r_o + r_i)} \sqrt{\frac{\mu_0 \ln\left[ 1.24 \times 10^7 \left(\frac{T_e^3}{n_e}\right)^{\frac{1}{2}} \right]}{\tau}}. \quad (2.48)$$

$$x_s(0) = 0, \ \dot{x}_s(0) = 0, \ \int_0^{t=0} I(t)\,dt = 0, \ I(0) = 0. \quad (2.26)$$

The energy equation follows the same derivation as the for the parallel plate version resulting in equation (2.28).

$$\int_0^t I(t) V_c\,dt = \int_0^t \frac{d}{dt}\left\{ \frac{1}{2}\left[ I(t) \right]^2 L_T(t) \right\} dt + \int_0^t R_T(t)\left[ I(t) \right]^2 dt + \int_0^t \frac{1}{2}\left[ I(t) \right]^2 \dot{L}_T(t)\,dt. \quad (2.28)$$

Substituting the coaxial inductance model and evaluating the left-hand-side integral using (2.29), results in the general coaxial energy equation

$$\frac{1}{2}CV_0^2 - \frac{1}{2}C\big[V_c(t)\big]^2 = \frac{1}{2}\big[I(t)\big]^2\left[L_c + L_e + \frac{\mu_0}{4\pi}\ln\left(\frac{r_o}{r_i}\right)x_s(t) + \mu_0\frac{\delta}{4\pi}\ln\left(\frac{r_o}{r_i}\right)\right] +$$

$$\int_0^t R_T(t)\big[I(t)\big]^2 dt + \int_0^t \frac{\mu_0}{4\pi}\ln\left(\frac{r_o}{r_i}\right)\big[I(t)\big]^2 \dot{x}_s(t)\,dt. \quad (2.50)$$

## a) Slug Operation

The generalized coaxial PPT electromechanical model can be easily adapted to the various operational modes of coaxial PPTs. A coaxial APPT can be modeled using a "slug" mass model with a mass loading parameter $\alpha = 1$. This slug model is also applicable for a GFPPT operating with minimal propellant gas expansion. Thus, the entire system of equations with its accompanying initial conditions can be written as

$$V_0 - \frac{1}{C}\int_0^t I(t)\,dt = I(t)\left\{R_c + R_e + R_{pe} + \frac{r_o - r_i}{\sigma_p \delta(r_o + r_i)}\right\} +$$

$$\left[L_c + L_e + \frac{\mu_0}{4\pi}\ln\left(\frac{r_o}{r_i}\right)x_s(t) + \mu_0\frac{\delta}{4\pi}\ln\left(\frac{r_o}{r_i}\right)\right]\dot{I}(t) + \frac{\mu_0}{4\pi}\ln\left(\frac{r_o}{r_i}\right)\dot{x}_s(t)I(t), \quad (2.51)$$

$$m_0\ddot{x}_s(t) = \frac{\mu_0}{4\pi}\ln\left(\frac{r_o}{r_i}\right)\big[I(t)\big]^2, \quad (2.52)$$

$$R_p = 2.57\frac{r_o - r_i}{T_e^{\frac{3}{4}}(r_o + r_i)}\sqrt{\frac{\mu_0\ln\left[1.24\times10^7\left(\frac{T_e^3}{n_e}\right)^{\frac{1}{2}}\right]}{\tau}}. \quad (2.48)$$

$$x_s(0) = 0,\ \dot{x}_s(0) = 0,\ \int_0^{t=0} I(t)\,dt = 0,\ I(0) = 0. \quad (2.26)$$

## b) Snowplow Operation

To model the majority of operational modes of coaxial GFPPTs, a current sheet mass that is a function of sheet position was employed. As was done in the case of the parallel plate snowplow model, this was done by using the mass distribution model with a mass distribution parameter, $\alpha < 1$. Using a mass distribution parameter equal to zero simulates a uniform mass distribution throughout the channel. Thus, the entire system of equations with its accompanying initial conditions is

$$V_0 - \frac{1}{C}\int_0^t I(t)\,dt = I(t)\left\{R_c + R_e + R_{pe} + \frac{r_o - r_i}{\sigma_p \delta(r_o + r_i)}\right\} +$$

$$\left[L_c + L_e + \frac{\mu_0}{4\pi}\ln\left(\frac{r_o}{r_i}\right)x_s(t) + \mu_0\frac{\delta}{4\pi}\ln\left(\frac{r_o}{r_i}\right)\right]\dot{I}(t) + \frac{\mu_0}{4\pi}\ln\left(\frac{r_o}{r_i}\right)\dot{x}_s(t)I(t),\,(2.53)$$

$$m(t)\ddot{x}_s(t) + \dot{m}(t)\dot{x}_s(t) = \frac{\mu_0}{4\pi}\ln\left(\frac{r_o}{r_i}\right)\left[I(t)\right]^2, \tag{2.54}$$

$$m(t) = m_0 + m_t\left[1 - \left[1 - \frac{x_s(t)}{l}\right]^{\frac{1}{1-\alpha}}\right], \tag{2.18}$$

$$R_p = 2.57\frac{r_o - r_i}{T_e^{\frac{3}{4}}(r_o + r_i)}\sqrt{\frac{\mu_0\ln\left[1.24\times10^7\left(\frac{T_e^3}{n_e}\right)^{\frac{1}{2}}\right]}{\tau}}. \tag{2.48}$$

$$x_s(0) = 0,\ \dot{x}_s(0) = 0,\ \int_0^{t=0} I(t)\,dt = 0,\ I(0) = 0. \tag{2.26}$$

## 2.3.  Electromechanical Model for an Applied Field PPT

In order to simulate an applied magnetic field PPT the generalized electromechanical PPT models must be modified. Specifically, external magnetic fields

applied parallel to the self-induced magnetic fields were modeled. The enclosed geometry of the coaxial PPT makes applying an azimuthal magnetic fields exceedingly difficult (Figure 2.12).
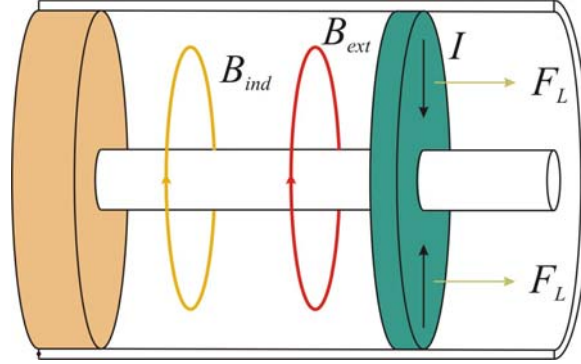


**Figure 2.12  Coaxial Applied Magnetic Field PPT**

Therefore, the applied field model was derived for the parallel plate geometry only.

For this initial control study, the applied magnetic field will be modeled as not exhibiting any mutual inductance with the PPT circuit. In the case that the field is applied by an electromagnet, the model would be inexact as the electromagnet's circuit would carry some mutual inductance with the discharging PPT circuit. To accurately model such a scenario would require modeling the external circuit through another circuit equation. The details of this are presented in Appendix A.

The derivation for the modified parallel plate PPT model is similar to the derivation for the general model, and begins with Faraday's law around the PPT circuit

$$V_c\left(t\right) = IR_T\left(t\right) + \frac{d}{dt}\left[\lambda_{PPT}\left(t\right)\right]. \tag{2.1}$$

$\lambda_{PPT}$ here is the total magnetic flux through the PPT system. This flux can be written in terms of the components of the PPT

$$\lambda_{PPT}\left(t\right) = \lambda_c\left(t\right) + \lambda_e\left(t\right) + \lambda_{pe}\left(t\right), \tag{2.2}$$

where the three terms on the right are, respectively, the magnetic flux due to the capacitor inductance, the wire and lead inductance and the flux through the electrode channel. Using the previous result for the self-induced magnetic field (2.9) and assuming the external magnetic field is applied throughout the electrode channel and current sheet, (2.2) may be written as

$$\lambda_{PPT}(t) = L_c I(t) + L_e I(t) + \left[ \mu_0 \frac{h}{w} x_s(t) + \mu_0 \frac{\delta}{2} \frac{h}{w} \right] I(t) +$$

$$\int_0^{x_s(t)} \int_0^h B_{ext}(t,x,y)\,dy\,dx + \int_{x_s(t)}^{x_s(t)+\delta} \int_0^h B_{ext}(t,x,y)\,dy\,dx, \qquad (2.55)$$

where $B_{ext}(t,x,y)$ is the magnitude of the external magnetic field. Assuming the applied field has negligible spatial gradient over the electrode channel region yields

$$\lambda_{PPT}(t) = L_c I(t) + L_e I(t) + \left[ \mu_0 \frac{h}{w} x_s(t) + \mu_0 \frac{\delta}{2} \frac{h}{w} \right] I(t) + h B_{ext}(t) \left[ x_s(t) + \delta \right]. \quad (2.56)$$

Substituting this into (2.1) gives the circuit equation for the modified system

$$V_c(t) = V_0 - \frac{1}{C}\int_0^t I(\tau)\,d\tau = I(t)\left( R_c + R_e + R_{pe} + R_p \right) +$$

$$\dot{I}(t)\left[ L_c + L_e + \mu_0 \frac{h}{w} x_s(t) + \mu_0 \frac{\delta}{2} \frac{h}{w} \right] + I(t)\mu_0 \frac{h}{w}\dot{x}_s(t) + h\frac{d}{dt}\left\{ B_{ext}(t)\left[ x_s(t) + \delta \right] \right\}. (2.57)$$

Notice that in comparing this equation with (2.27), the only modification is the addition of the later term.

The dynamic equation derivation follows the general model with the only deviation arising due to the difference in the magnetic field throughout the current sheet. Taking the result from the parallel plate model and applying superposition gives the magnetic field throughout the PPT

$$\mathbf{B}(t,x)=\begin{cases}\mu_0\dfrac{I(t)}{w}\hat{\mathbf{y}}+B_{ext}(t)\hat{\mathbf{y}}, & 0<x<x_s(t)\\[2mm]\mu_0\dfrac{I(t)}{w}\left[1-\dfrac{x-x_s(t)}{\delta}\right]\hat{\mathbf{y}}+B_{ext}(t)\hat{\mathbf{y}}, & x_s(t)<x<x_s(t)+\delta.\\[2mm]B_{ext}(t)\hat{\mathbf{y}}, & x>x_s(t)+\delta\end{cases}\qquad(2.58)$$

With a uniform current density throughout the current sheet

$$\mathbf{j}(t)=-\frac{I(t)}{w\delta}\hat{\mathbf{z}},\qquad(2.7)$$

the Lorentz force acting on the current sheet will be

$$\mathbf{F}(t)=\iiint\limits_{\substack{current\\ sheet}}\mathbf{j}(t)\times\mathbf{B}(t,x)\,dV=\frac{I(t)h}{\delta}\hat{\mathbf{x}}_s\int\limits_{x_s(t)}^{x_s(t)+\delta}\left\{\mu_0\frac{I(t)}{w}\left[1-\frac{x-x_s(t)}{\delta}\right]+B_{ext}(t)\right\}dx=$$

$$\left\{\frac{1}{2}\mu_0\frac{h}{w}\left[I(t)\right]^2+hI(t)B_{ext}(t)\right\}\hat{\mathbf{x}}_s.\qquad(2.59)$$

Substituting this into Newton's second law of motion yields

$$\frac{d}{dt}\left[m(t)\dot{\mathbf{x}}_s(t)\right]=\frac{1}{2}\mu_0\frac{h}{w}\left[I(t)\right]^2+hI(t)B_{ext}(t).\qquad(2.60)$$

Taking this dynamic equation with the circuit equation (2.57), the mass distribution model (2.18), the resistance model (2.21)-(2.24) and initial conditions (2.26) yields the parallel plate model modified to include an externally applied magnetic field.

$$V_0-\frac{1}{C}\int_0^t I(\tau)\,d\tau=I(t)\left(R_c+R_e+R_{pe}+R_p\right)+\left[L_c+L_e+\mu_0\frac{h}{w}x_s(t)+\mu_0\frac{\delta}{2}\frac{h}{w}\right]\dot{I}(t)+$$

$$\mu_0\frac{h}{w}\dot{x}_s(t)I(t)+\dot{x}_s(t)hB_{ext}(t)+x_s(t)h\dot{B}_{ext}(t),\qquad(2.57)$$

$$\frac{d}{dt}\left[m(t)\dot{\mathbf{x}}_s(t)\right]=\frac{1}{2}\mu_0\frac{h}{w}\left[I(t)\right]^2+hI(t)B_{ext}(t),\qquad(2.60)$$

$$m(t) = m_0 + m_t \left[ 1 - \left[ 1 - \frac{x_s(t)}{l} \right]^{\frac{1}{1-\alpha}} \right],$$
(2.18)

$$R_p = 8.08 \frac{h}{T_e^{\frac{3}{4}} w} \sqrt{\frac{\mu_0 \ln \left[ 1.24 \times 10^7 \left( \frac{T_e^3}{n_e} \right)^{\frac{1}{2}} \right]}{\tau}}$$
(2.48)

$$x_s(0) = 0, \ \dot{x}_s(0) = 0, \ \int_0^{t=0} I(t) dt = 0, \ I(0) = 0.$$
(2.26)

In the case of a constant external magnetic field, the final term of (2.57) will be zero. This model was numerically integrated using the same method described in chapter 3 to arrive at solutions for $I(t)$ and $x_s(t)$.

The energy equation for the circuit is again of interest with this modified model and can be derived from the circuit equation following the procedure used for the general model. Multiplying (2.57) by $I(t)$ and rearranging the terms gives the power equation for the modified circuit,

$$V_c(t) I(t) = R_T \left[ I(t) \right]^2 +$$
$$\frac{d}{dt} \left\{ \frac{1}{2} L_T(t) \left[ I(t) \right]^2 \right\} + \frac{1}{2} \dot{L}_T(t) \left[ I(t) \right]^2 + h \frac{d}{dt} \left[ x_s(t) B_{ext}(t) \right] I(t).$$
(2.61)

Substituting for the current in the capacitor power term on the right hand side

$$I(t) = -C \frac{dV_c(t)}{dt}$$
(2.29)

and integrating over time yields,

$$\frac{1}{2} C V_0^2 - \frac{1}{2} C \left[ V_c(t) \right]^2 = \int_0^t R_T \left[ I(\tau) \right]^2 d\tau +$$

49

$$\frac{1}{2}L_T(t)\big[I(t)\big]^2 + \int_0^t \frac{1}{2}\dot{L}_T(\tau)\big[I(\tau)\big]^2 d\tau + h\int_0^t I(\tau)\frac{d}{dt}\big[x_s(\tau)B_{ext}(\tau)\big]d\tau. \qquad (2.62)$$

This modified energy equation is the same as the original equation apart from the last term. This term accounts for the work performed by the circuit on the current sheet mass due to the external magnetic field and the energy stored in the circuit magnetic field due to the changing flux of the external magnetic field.

$$h\int_0^t I(\tau)\frac{d}{dt}\big[x_s(\tau)B_{ext}(\tau)\big]d\tau = h\int_0^t \dot{x}_s(\tau)B_{ext}(\tau)I(\tau)d\tau + h\int_0^t x_s(\tau)\dot{B}_{ext}(\tau)I(\tau)d\tau \;(2.63)$$

# Chapter 3

# Numerical Implementation, Software Implementation and Model Validation

This chapter discusses several practical issues pertaining to the one dimensional PPT models. Here, the numerical method employed in solving the model equations is presented. Furthermore, the GUI software environment developed to change model parameters and view the solution results is described. Finally, the model is validated for the case of ablative PPTs by comparison with the LES-6 and LES-8/9 PPTs.

## 3.1. Numerical Implementation

The second order systems of coupled nonlinear integro-differential equations were solved numerically for both coaxial [Equations (2.49), (2.45), (2.18), (2.48) and (2.26)] and parallel plate geometries [Equations (2.27), (2.31), (2.18), (2.25) and (2.26)] and slug and snowplow operating conditions. To accomplish this, each set of equations were written as a system of four first-order differential equations through the following state space variables

$$x_1(t) = x_s(t), \tag{2.64}$$

$$x_2(t) = \int_0^t I(\tau)d\tau, \tag{2.65}$$

$$x_3(t) = \dot{x}_s(t), \tag{2.66}$$

51

$$x_4(t) = I(t). \tag{2.67}$$

In this state space form the parallel plate slug model equations become

$$\dot{x}_1(t) = x_3(t), \tag{2.68}$$

$$\dot{x}_2(t) = x_4(t), \tag{2.69}$$

$$\dot{x}_3(t) = \frac{1}{2}\frac{L'_{pe}}{m_0}\left[x_4(t)\right]^2, \tag{2.70}$$

$$\dot{x}_4 = \frac{-\left(\frac{1}{C}\right)x_2(t) - \dot{L}_T(t)x_4(t) - R_T x_4(t) + V_0}{L_T(t)}, \tag{2.71}$$

$$x_1(0) = 0, \; x_2(0) = 0, \; x_3(0) = 0, \; x_4(0) = 0, \tag{2.72}$$

where $R_T = R_c + R_e + R_{pe} + R_p$, $L_T(t) = L_c + L_e + L_{pe}(t)$ and $R_p$ is given by (2.48) and $L_{pe}(t)$ is given by (2.13).

The above nonlinear ordinary differential equation (ODE) system was integrated numerically by implementing MATLAB's® nonlinear ODE solvers. For initial numerical solutions, LES 6 PPT parameters were used (Table 1). It was initially thought that there would be possible issues with ODE stiffness and as such, the initial solvers implemented were ode23s and ode15s. The validity and accuracy of these methods was checked by verifying that system energy was conserved for both the general model and the modified model. Since the circuit equation is a statement of energy conservation for the electrical system this is a valid requirement for an acceptable method. Using the terms in (2.30) the energy on the capacitor is given by

$$E_c(t) = \frac{1}{2}C\left[V_c(t)\right]^2, \tag{2.73}$$

52

where $V_c(t)$ is the voltage on the capacitor. The voltage on the capacitor was calculated at each timestep using

$$V_c(t) = V_0 - \frac{1}{C}\int_0^t I(t)\,dt = V_0 - \frac{1}{C}x_2(t). \tag{2.74}$$

The energy dissipated by ohmic heating is given by

$$E_\Omega(t) = \int_0^t R_T(\tau)\left[I(\tau)\right]^2 d\tau = \int_0^t R_T(\tau)\left[x_4(t)\right]^2 d\tau. \tag{2.75}$$

The integral appearing in this equation was solved numerically using a trapezoidal sum. The energy stored in the magnetic field is given by

$$E_B(t) = \frac{1}{2}\left[L_c + L_e + \mu_0\frac{h}{w}x_s(t)\right]\left[I(t)\right]^2 = \frac{1}{2}\left[L_c + L_e + \mu_0\frac{h}{w}x_1(t)\right]\left[x_4(t)\right]^2. \tag{2.76}$$

Finally, the energy given to the accelerated current sheet is given by

$$E_{KE}(t) = \frac{1}{2}m_0\left[V(t)\right]^2 = \frac{1}{2}m_0\left[x_3(t)\right]^2. \tag{2.77}$$

The modified model has an extra term in its energy equation (2.62) in comparison with the general model energy equation. This term accounts for the work performed by the circuit on the current sheet mass due to the external magnetic field and the energy stored in the circuit magnetic field due to the changing flux of the external magnetic field.

$$h\int_0^t I(\tau)\frac{d}{dt}\left[x_s(\tau)B_{ext}(\tau)\right]d\tau = h\int_0^t x_3(\tau)x_4(\tau)B_{ext}(\tau)d\tau + h\int_0^t x_1(\tau)x_4(\tau)\dot{B}_{ext}(\tau)d\tau \tag{2.78}$$

Summing these components at each timestep yields the total energy throughout the discharge. By choosing a sufficiently tight tolerance setting both stiff ODE solver methods yielded solutions that conserved the system energy (Figure 4.1 and Figure 4.2).
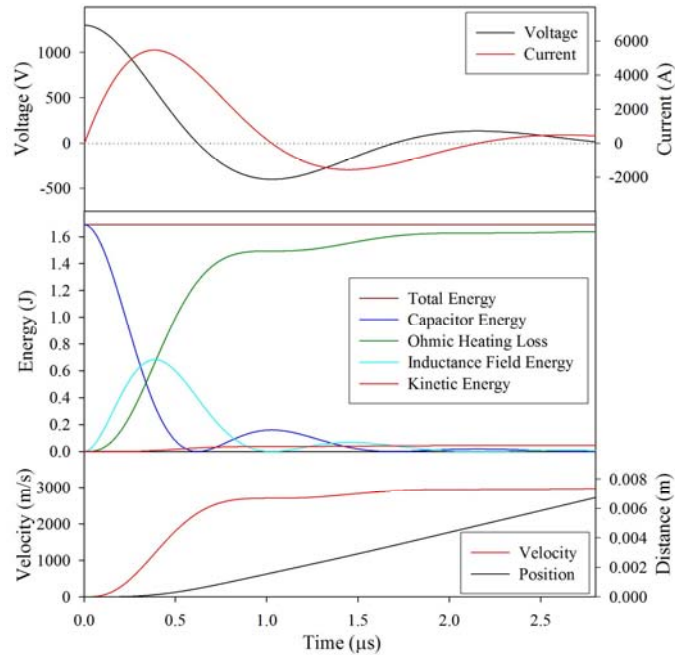
**Figure 3.1  General model simulation output using LES-6 thruster parameters.**
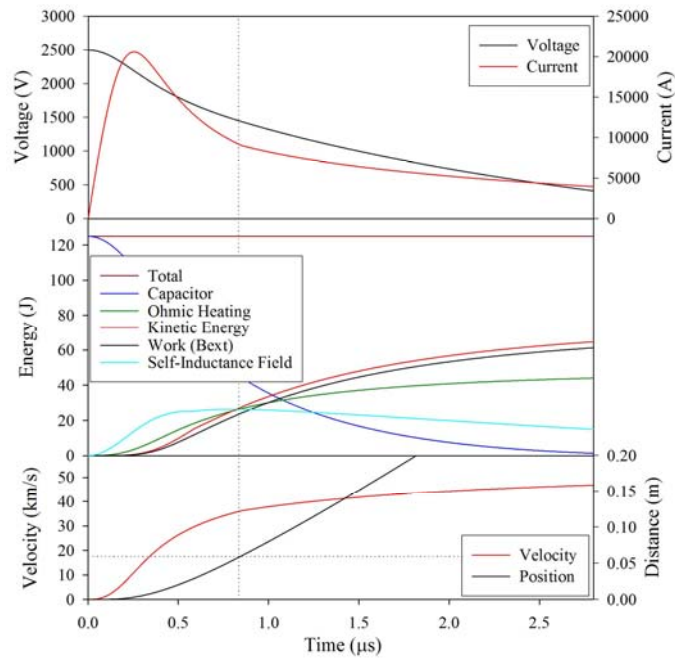


**Figure 3.2  Nominal applied magnetic field PPT simulation (Bext =0.3 T).**

In addition to the stiff solver, the non-stiff solvers; ode23, ode45 and ode113, were implemented in numerically integrating the systems.  If the system has stiffness

54

issues, these solvers would be very inefficient arriving at a solution, requiring a significant number of timesteps and run time to solve. However, these solvers were generally found to integrate the system with fewer timesteps than the stiff solvers, leading to the conclusion that the system is not particularly stiff. The solver chosen for use throughout the thesis was the one that conserved system energy while minimizing the tolerance, timesteps, and computer run time. This was determined to be ode45 at absolute and relative tolerance levels of 1e-6. Ode45 is a single step method based on an fourth and fifth order explicit Runge-Kutta formula called the Dormand-Prince pair [Dormand et al., 1980].

Two solver schemes were implemented in solving the system. The MATLAB® ODE solvers were applied in an automatic way by allowing them to determine the length of each timestep. Depending on the input tolerance level, the solver automatically determines the length of each timestep based upon the dynamics of the ODE at that timestep. This results in a solution with the fewest number of calculations and timesteps while maintaining the accuracy determined by the tolerance level. However, as a way to implement more control over the solution, another method, utilized in the work by Demetriou et al. [2003], was also implemented. This method requires user inputs for the number of timesteps, tolerance and number of integration points in each timestep. The method divides up the time interval into subintervals each the length of the timestep. A MATLAB® ODE solver is applied over this interval using the solution from the last timestep for its initial values. The solution is calculated over the timestep subinterval at a number of points equal to the user input number of integration points. The final output is taken as the solution at the endpoints of each subinterval. In addition to giving the user

more control in choosing the timestep length, this method will also generally give a more accurate integration. The major drawback with this method is the computational run time, taking up to minutes to arrive at a solution versus seconds with the automatic solution method.

In addition to the energy being calculated, various other thruster performance parameters were determined or calculated. The exhaust velocity was taken to be the velocity at which the position of the current sheet was equal to the length of the thruster. This system state is defined as

$$\dot{x}_e = \dot{x}_s\left(t^*\right), \tag{2.79}$$

where

$$t^*: \quad x\left(t^*\right) = l. \tag{2.80}$$

The specific impulse was calculated from the exhaust velocity as

$$I_{sp} = \frac{\dot{x}_e}{g}, \tag{2.81}$$

where $g$ is the acceleration of gravity at sea level. To calculate the impulse bit, the impulse acting on the current sheet was calculated as a function of time through

$$I_{bit}\left(t\right) = \int_0^t \frac{1}{2}\mu_0 \frac{h}{w}\left[I\left(t\right)\right]^2 d\tau. \tag{2.82}$$

This integral was solved numerically using the trapezoidal summation and the impulse bit for the simulation was taken to be the impulse at the current sheet exit time.

## 3.2.    Software Implementation

The general PPT model has the potential for 21 input parameters. With such a significant number of model inputs, it was decided that a graphical user interface (GUI)

56

application should be developed to provide an easy means for changing model inputs and visualizing simulation results. To accomplish this, MATLAB's® Graphical User Interface Development Environment (GUIDE) was utilized. GUIDE provides all the necessary tools to design and write the code for a MATLAB® GUI. This allowed all of the model inputs and resulting plots to be displayed in the same window. Figure 4.3 displays the PPT model GUI.
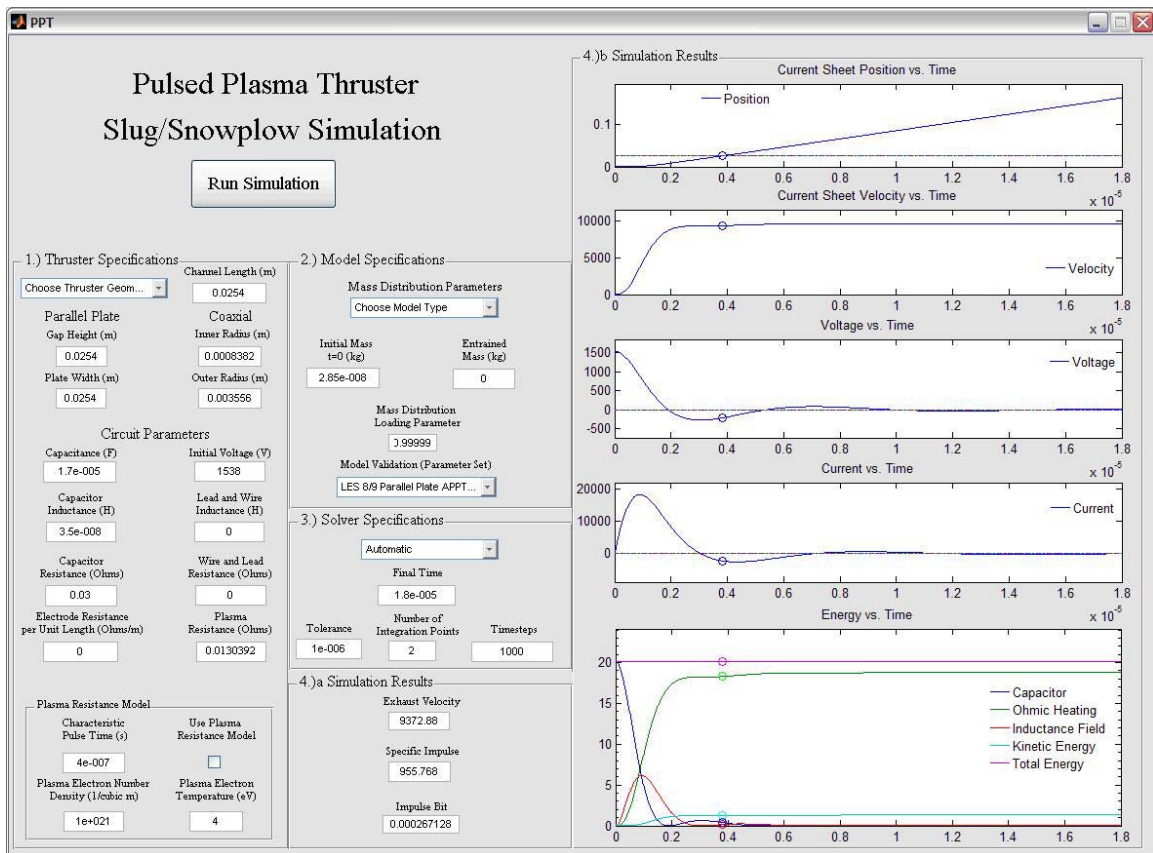


**Figure 3.3  MATLAB® one dimensional PPT model GUI.**

In the first user inputs section, the "Thruster Specifications" as user can change the geometry settings, the circuit parameters, and plasma resistance model parameters. Additionally, a user can turn the plasma resistance model off using a user input value of resistance. In the second section, "Model Specifications" a user defines what type of

model will be simulated; slug, snowplow (constant density distribution) and snowplow (variable density distribution).  Additionally, here a user can simulate certain thrusters, whose model parameter sets have been previously entered.  The last user input section, "Solver Specifications" allows a user control over how the system is solved.  The user can choose from the 'automatic' MATLAB® solver and the 'manual' solver.  The automatic solver only has options for changing the tolerance.  Using the manual solver a user can change the tolerance, number of timesteps and the number of integration points throughout each timestep.  Lastly, here a user specifies the total time domain the system is solved over.

## 3.3.    General Model Validation

The general model was validated for the case of a parallel plate ablative PPT (Table 4.1).

**Table 3.1 General Model Validation**

|          | Parallel Plate | | Coaxial | |
|----------|------|----------|------|----------|
|          | Slug | Snowplow | Slug | Snowplow |
| Ablative | yes  | no       | no   | no       |
| Gas-Fed  | -    | -        | no   | no       |

In order to validate the general model, simulation results were compared with data (Table 4.2) from two parallel plate thrusters; the LES 6 [Vondra et al., 1970 and 1971] and the LES 8/9 [Vondra et al., 1973], [Leiweke, 1996].

**Table 3.2 Experimental Parallel Plate PPT Data**

| Thruster | LES-6 PPT | LES-8/9 PPT |
|----------|-----------|-------------|
| Initial Voltage (V) | 1360 | 1538 |
| Capacitance (μF) | 2 | 17 |
| Capacitor Resistance (mΩ) | 30 | 30 |
| Initial Inductance (nH) | 34 | 35 |
| Gap Width (cm) | 3 | 2.54 |

| Plate Width (cm) | 1 | 2.54 |
| --- | --- | --- |
| Channel Length (cm) | 0.6 | 2.54 |
| Mass Bit (μg) | 10 | 28.5 |
| Pulse Time (μs) | 0.4 | 1.0 |
| Plasma Temperature (eV) | 1.5 | 5 |
| Electron Density (m$^{-3}$) | 1e21 | 1e21 |

It should be noted that the value of capacitor and wire and lead resistance for the LES 8/9 was determined from the measured total resistance of 45 mΩ and a plasma resistance on the order of 15 mΩ [Leiweke, 1996]. The average plasma temperature for the LES 8/9 was estimated based on langmuir probe plume measurements [Gatsonis et al., 2001].

Using this data as inputs into our model, simulation results were compared with experimental data. The current and voltage waveforms for the LES-6 PPT were found in Waltz [1969]. In this work, a voltage measurement was taken as closely as possible to the capacitor terminals. Because the capacitor inherently has some internal resistance and inductance, this measurement does not correspond to an actual capacitor voltage measurement (Figure 4.4).
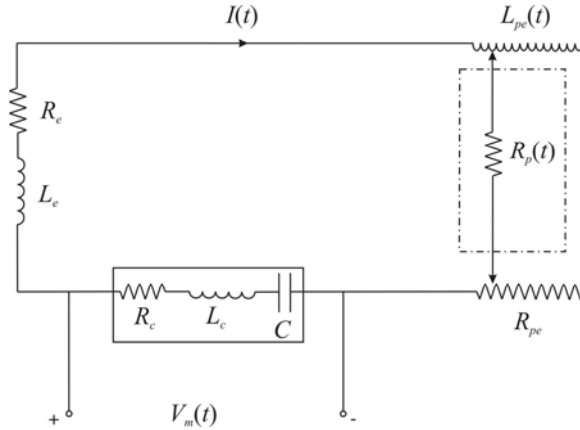


**Figure 3.4  LES-6 circuit with voltage measurement.**

However, from this data the actual circuit current was found by solving the following second-order ODE

$$CV_m(t) = -I(t) - R_c C\dot{I}(t) - L_c C\ddot{I}(t).$$ (2.83)

59

This experimental data was then plotted along with the simulation data for comparison (Figure 4.5).
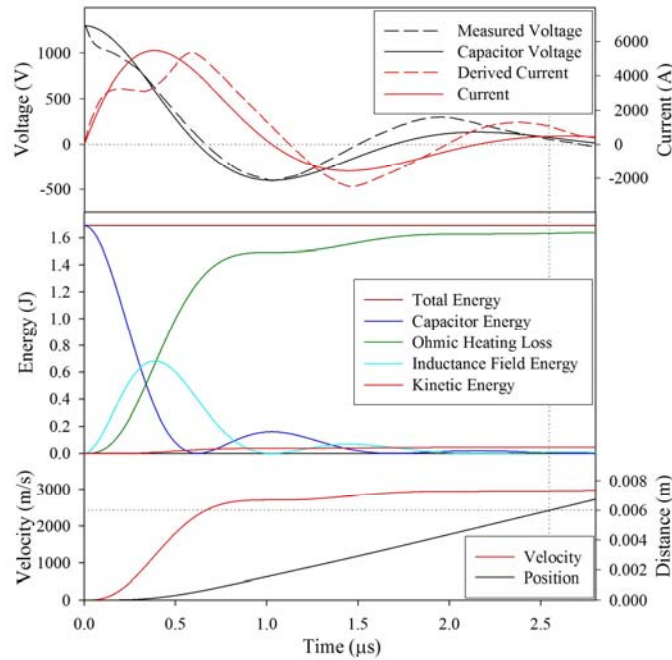


**Figure 3.5  LES-6 experiment and simulation comparison.**

The vertical dotted line indicates the time at which the current sheet exits the thruster for the simulation.  The disagreement between the experiment and simulation can be mainly attributed to the constant plasma resistance in the model.  This value was calculated by the plasma resistance model to be 0.074 $\Omega$.  In the real thruster, the plasma resistance will vary as the plasma is being formed and as the electron temperature and number density change.  This modeling issue shows itself the most at the beginning of the discharge while the plasma is being formed and is evident in the initial "hitch" in the derived current waveform.  According to Waltz [1969] the plasma resistance at this time achieves a maximum of 0.3 $\Omega$.  Despite this, the overall dynamics of the PPT LCR circuit appear to be well matched.  Table 4.3 compares the exit velocity, specific impulse and impulse bit of the actual thruster and this simulation [Vondra et al., 1970]

**Table 3.3  LES-6 simulation validation.**

|                          | Experimental | Simulation |
|--------------------------|--------------|------------|
| Exit Velocity (ms$^{-1}$) | 3000         | 2975       |
| Specific Impulse (s)     | 312          | 303        |
| Impulse Bit (μN-m)       | 32           | 30         |

The slight underprediction in performance values is likely due a combination of a variable plasma resistance and the presence of gas dynamic effects in the real thruster.

For the LES 8/9, the experimental voltage waveform data was found published in Leiweke [1996].  Like the LES-6, this voltage measurement did not correspond exactly with the capacitor voltage due to the internal capacitor resistance and inductance.  This experimental waveform was plotted along with the simulation data for comparison (Figure 4.6).  Though no current waveform could be located throughout literature, the experimental peak current of 19 kA was found published in Vondra et al. [1973].
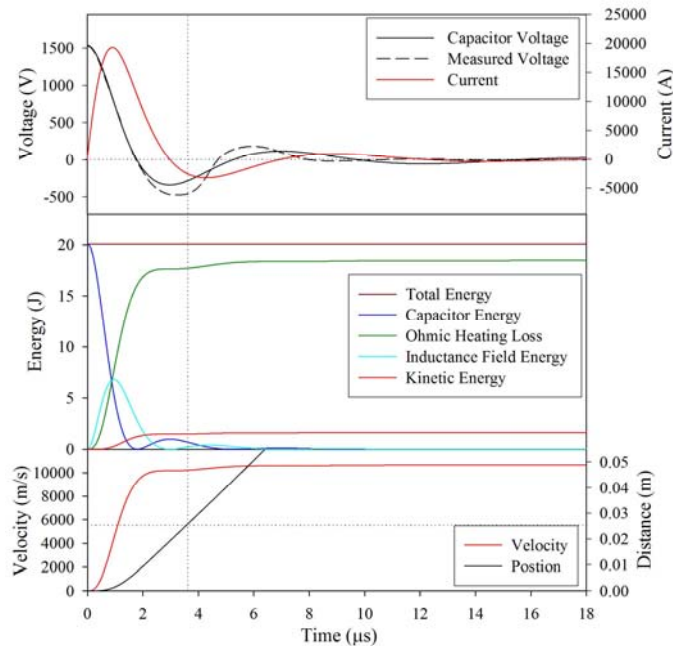


**Figure 3.6  LES-8/9 experiment and simulation comparison.**

61

The vertical dotted line again indicates the time at which the current sheet exits the thruster for the simulation. Like for the LES-6, the overall dynamics of the LCR circuit appear to be fairly well matched. Though there is an under prediction in the voltage reversal, the maximum simulation current of 20 kA compares very well with the actual thruster (19 kA). The plasma resistance model gives a value of 0.011 $\Omega$. Table 4.4 compares the exit velocity, specific impulse and impulse bit of the actual LES-8/9 and the simulation [Vondra et al., 1973].

**Table 3.4  LES-8/9 simulation validation.**

|  | Experimental | Simulation |
| --- | --- | --- |
| Exit Velocity (ms$^{-1}$) | 9810 | 9674 |
| Specific Impulse (s) | 1000 | 986 |
| Impulse Bit (µN-m) | 300 | 276 |

The comparison here is very similar to the LES-6. Again, the slight underprediction by the model may be attributed to a variable plasma resistance and the presence of gas dynamic effects in the real thruster. Looking at the results of both simulations, it can be concluded that the one-dimensional model predicts parallel plate PPT performance very well

### 3.4.    Modified Model Validation

The modified model was validated for the case of a constant magnetic field applied by permanent magnets. Modified model simulation results were compared with data from the 1984 UOT parallel plate thruster. This data set was chosen due to its relative completeness and also because permanent magnets were utilized in applying the external magnetic field. This was the simplest case to validate and therefore provided a solid baseline comparison. For model inputs, the data presented in Table 2.1 was utilized. This data set was complete excepting resistance data. The plasma resistance

model was unable to be utilized due to a lack of plasma temperature and electron density data for a high energy (125 J) PPT.  Therefore, to complete the data set, the capacitor resistance and plasma resistance were set to 0.03 Ω and 0.015 Ω, respectively, for all the simulations.  These values correspond closely to the values found in the LES-6 and LES-8/9 thrusters.  For each simulation, the external magnetic field was applied over the first 1.75 cm of the electrode length.  This was in agreement with the experimental setup described in the paper [Takegahara et al., 1984].  The mass distribution was modeled in each simulation as a slug distribution with all the mass contained within the current sheet at $t = 0$.

Figures 4.6 and 4.7 compare the simulation and experiment results [Takegahara et al., 1984] for specific impulse, thrust efficiency and impulse bit.
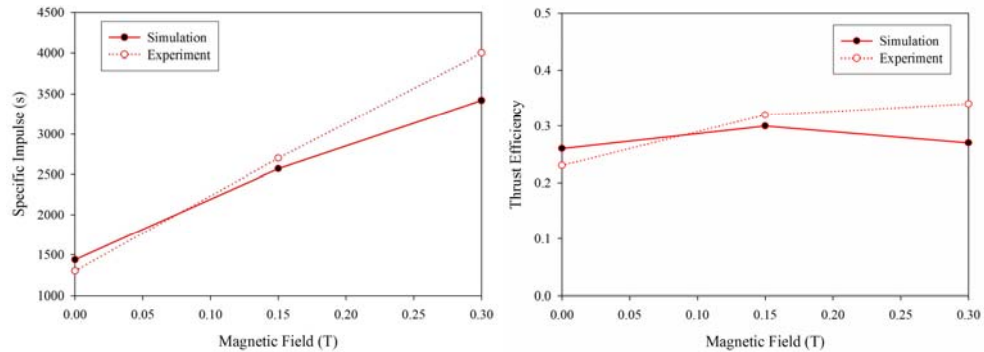


**Figure 3.7  Specific impulse and thrust efficiency validation comparison.**
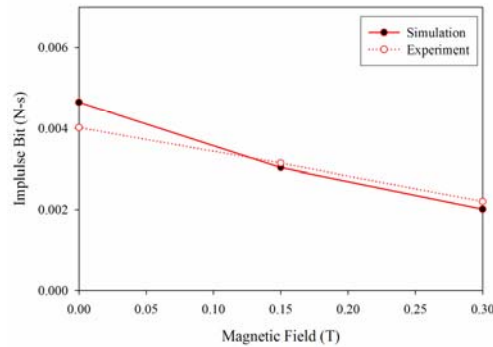


**Figure 3.8  Impulse bit validation comparison.**

While the simulation results show good overall agreement with the experimental values, there did appear to be a general divergence between the two. As can be seen in the figures, the simulation tends to over-predict the PPT performance with no applied magnetic field, under-predict at the highest field value and give generally very good agreement at the intermediate value. This deviation is most certainly due to the model not accounting for gas dynamic effects. As discussed in Chapter 1, an accelerating applied magnetic field has the effect of causing a parallel plate PPT to operate electromagnetically versus gas dynamically. In these validation simulations the entire measured mass bit was assumed accelerated electromagnetically. In reality, only a fraction of the mass would be ionized and accelerated electromagnetically. The remaining fraction of mass, would gas dynamically expand away from the thruster as a cloud of neutrals. This phenomenon was particularly prevalent in the thruster utilized for this validation. This is evidenced by the large decrease in mass bit (300 to 60 μg) with accompanying increase in applied field strength. This conclusion would lead one to wonder why the simulation was not more accurate at the higher value of applied magnetic field. The likely answer to this is an under-estimation of the circuit resistance (capacitor and plasma). Using a lower value of resistance in the simulation would have the effect of shifting all the results up. This would cause a better matching of simulation and experiment at the higher value of applied magnetic field and an increasing divergence with decreasing applied field strength. However, despite this digression, the modified model appears to, quite satisfactorily; predict the performance of a parallel plate PPT under the influence of a constant magnetic field applied by permanent magnets.

# Chapter 4

# Control Strategy and Analysis

The overall objective of this work is the development of a control scheme to optimize PPT performance. In this study, an open-loop flow controller was investigated, developed and applied. An open-loop flow control system consists of a dynamic flow model, a control objective, a flow actuator and an open-loop controller (Figure 5.1). The actuator is some type of model input that can be utilized to control or manipulate the model outputs.
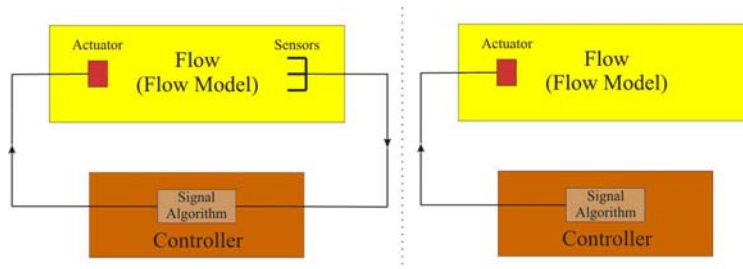


**Figure 4.1  Closed-loop and open-loop flow control.**

A closed-loop or feedback flow control system consists of a dynamic flow model, a control objective, flow actuator, flow sensor (model outputs) and a controller which commands the flow actuator in response to flow sensor outputs.

## 4.1.    Control Objective and System

There are a number of PPT performance parameters that could be optimized. These include, but are not limited to, specific impulse, impulse bit, thrust efficiency and

thrust-to-power. The specific impulse and thrust efficiency were chosen for optimization based on the current trends in PPT use on small satellites. On these satellites, an advantage PPTs inherently have is in their small impulse bits. As such, increasing the impulse bit will not be specifically addressed in this thesis. A high specific impulse on the other hand is desirable as it reduces the propellant mass needed to satisfy the mission $\Delta$V requirements.

The thrust efficiency of these devices is significantly lower than other electric propulsion devices and offers considerable opportunity for improved performance. Previous flight qualified PPTs have produced thrust efficiencies between 0.06 and 0.13 [Myers et al., 1994]. However, Burton et al. [1998] estimated that rectangular and coaxial PPTs have a maximum possible efficiency of 0.44 and 0.60, respectively. The thrust efficiency is given as the ratio of directed exhaust kinetic energy to energy initially stored on capacitor

$$\eta_t = \frac{(KE)_e}{E_0} = \frac{\frac{1}{2}m_e\dot{x}_e^2}{\frac{1}{2}CV_0^2} = \frac{m_e\dot{x}_e^2}{CV_0^2}.$$

(3.1)

The specific impulse can also be written in terms of the mass-averaged exhaust velocity as

$$I_{sp} = \frac{\dot{x}_e}{g}.$$

(2.81)

This shows that the specific impulse and thrust efficiency will be maximized by maximizing the thruster exhaust velocity. Accordingly, the control objective is an increase or maximization of thruster exhaust velocity over nominal operating conditions.

The flow actuator is the element of the control system that affects the model or device in such a way as to manipulate it to produce some desired output.  An externally applied magnetic field was chosen to accomplish this task.  It has recently been suggested in literature that externally applied magnetic fields will increase PPT performance [Burton et al., 1998], [Ziemer et al., 1999].  Furthermore, a group at the University of Tokyo successfully utilized both permanent magnets and electromagnets to apply external magnetic fields to parallel plate and coaxial laboratory PPTs [Kimura et al., 1978 and 1979].  Their experiments with the parallel plate PPTs show an increase in specific impulse and thrust efficiency with the application of self-field augmenting external magnetic fields [Takegahara et al., 1984].  Lastly, an external magnetic field can be introduced to the general one-dimensional PPT model with relative ease through the circuit equation.   One drawback of external magnetic fields is the difficulty in implementing them on coaxial PPTs.   While parallel plate PPTs can be augmented with magnetic fields quite readily, coaxial geometries are much less conducive to externally applied magnetic fields (Figure 2.10).  Because of this, the remainder of this thesis will focus on the parallel plate geometry.  In parallel plate PPTs, Lorentz force accelerating or retarding fields may be applied with permanent magnets (Figure 5.2) or electromagnets
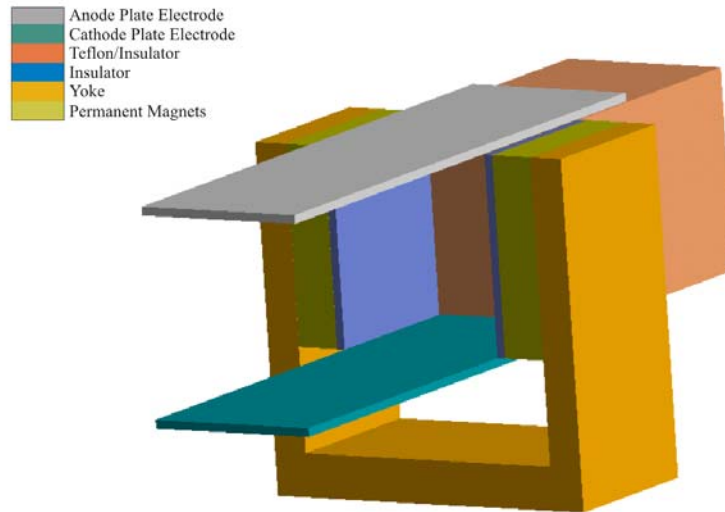
**Figure 4.2  Parallel plate PPT with external magnetic field applied via permanent magnets.**

The controller is central to the control system, as it carries out the control strategy by operating the flow actuators.  Three configurations of control were identified for the possibilities of simulation; open-loop constant input, open-loop variable input, and close-loop control.  In open-loop control, the command signal sent to the actuator by the controller can be either a constant value or a function of time.  In closed-loop control, the command signal is a function of the sensor outputs.  In this initial control study, an open-loop controller having constant applied magnetic field strength was examined.  Despite this, all three will be briefly described here.  Open-loop constant input control represents the simplest case that could be applied.  In this case, a constant magnitude magnetic field is applied over a length of the PPT channel.  This field may be applied either with permanent magnets or electromagnets.  An electromagnet may be utilized in this case by the coupling of an external LCR circuit with the PPT circuit as seen in Figure 5.3.
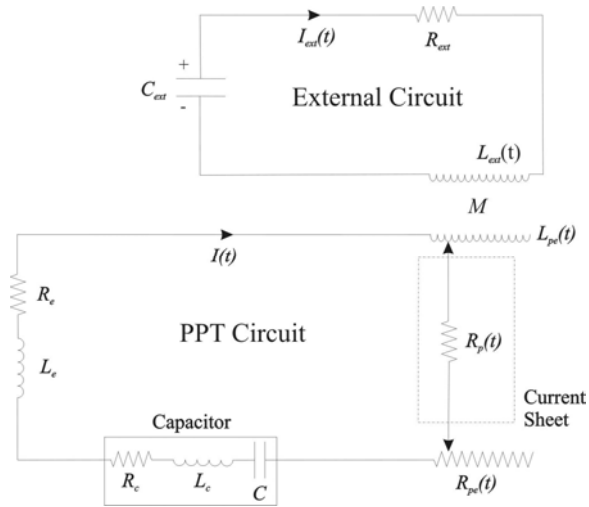
**Figure 4.3 Open-loop controller using coupled external LCR circuit.**

The external LCR circuit must have a discharge time much greater than the PPT circuit discharge time for the applied magnetic field to be quasi-static throughout the discharge. A time-variable open-loop controller could be implemented by applying an external magnetic field which varies over the length of the thruster channel through the use of a permanent magnet. Alternatively, this controller could also be implemented by utilizing an LCR circuit with a discharge time on the same order as the PPT discharge time. A closed-loop controller could be applied through the use of a similar coupled external circuit except, in this case, the capacitor would be replaced with a controllable voltage or current source (Figure 5.4). The models, which arise in the case of external circuits, are presented in Appendix A.
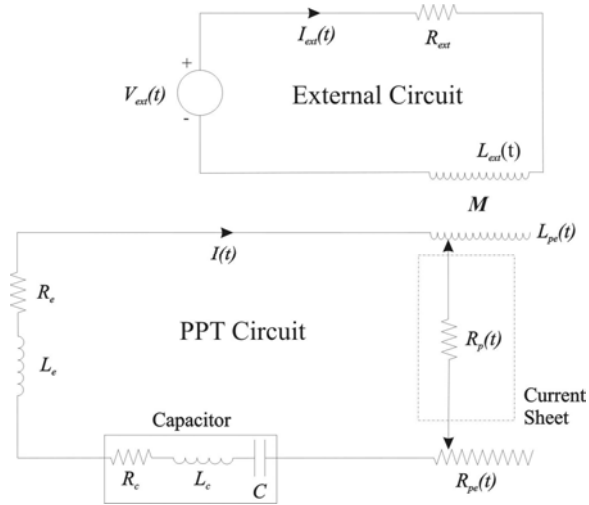
**Figure 4.4 Closed-loop controller using coupled external circuit with voltage source.**

## 4.2. Control Analysis

With the above model validated for the case of a constant applied magnetic field, it is of interest from a controls engineering standpoint to analyze the resulting nonlinear dynamic system. Using the previously defined state-space variables (2.64)-(2.67), and assuming the plasma resistance is constant, the above modified model can be written in state space as

$$\dot{x}_1 = x_3, \tag{3.2}$$

$$\dot{x}_2 = x_4, \tag{3.3}$$

$$\dot{x}_3 = \frac{1}{2}\mu_0 \frac{h}{mw}x_4^2 - \frac{\dot{m}}{m}x_3 + \frac{h}{m}x_4 B_{ext}, \tag{3.4}$$

$$\dot{x}_4 = \frac{V_0 - \left(\frac{1}{C}\right)x_2 - \mu_0 \frac{h}{w}x_3 x_4 - R_T x_4 - x_3 h B_{ext} - x_1 h \dot{B}_{ext}}{L_T(x_1)}, \tag{3.5}$$

where $R_T = R_c + R_e + R_{pe} + R_p$ and $L_T(x_1) = L_c + L_e + \mu_0 \frac{h}{w}x_1$.

Defining the state vector field, the input vector field and the drift vector field, respectively,

$$\mathbf{x}_{st}(t) = \begin{bmatrix} x_1(t) \\ x_2(t) \\ x_3(t) \\ x_4(t) \end{bmatrix}, \tag{3.6}$$

$$\mathbf{g}_1(\mathbf{x}(t)) = \begin{bmatrix} 0 \\ 0 \\ -\dfrac{h}{m} x_4(t) \\ -\dfrac{x_3(t)h}{L_c + L_e + \mu_0 \dfrac{h}{w} x_1(t)} \end{bmatrix}, \tag{3.7}$$

$$\mathbf{g}_2(\mathbf{x}(t)) = \begin{bmatrix} 0 \\ 0 \\ 0 \\ -\dfrac{x_1(t)h}{L_c + L_e + \mu_0 \dfrac{h}{w} x_1(t)} \end{bmatrix}, \tag{3.8}$$

$$\mathbf{f}(\mathbf{x}(t)) = \begin{bmatrix} x_3(t) \\ x_4(t) \\ \dfrac{1}{2}\mu_0 \dfrac{h}{mw}\left[x_4(t)\right]^2 - \dfrac{\dot{m}}{m} x_3(t) \\ \dfrac{V_0 - \left(\dfrac{1}{C}\right)x_2(t) - \mu_0 \dfrac{h}{w} x_3(t)x_4(t) - R_T(t)x_4(t)}{L_c + L_e + \mu_0 \dfrac{h}{w} x_1(t)} \end{bmatrix}, \tag{3.9}$$

$$u(t) = B_{ext}(t) \tag{3.10}$$

the above state space can be written as

$$\dot{\mathbf{x}}(t) = \mathbf{f}(\mathbf{x}(t)) + \mathbf{g}_1(\mathbf{x}(t))u(t) + \mathbf{g}_2(\mathbf{x}(t))\dot{u}(t), \tag{3.11}$$

71

Since only the case of a constant magnetic field has been validated and in order to help simplify this analysis, the time derivative term appearing in the numerator in (3.5), will be dropped resulting in the following state space system

$$\dot{\mathbf{x}}(t) = \mathbf{f}(\mathbf{x}(t)) + \mathbf{g}_1(\mathbf{x}(t))u. \tag{3.12}$$

In evaluating the equilibrium points in the drift vector field, $\mathbf{f}(\mathbf{x}(t))$, it can be easily seen that this system is in equilibrium at the following points

$$\mathbf{x}_e(t) = \begin{bmatrix} x_1(t) \\ V_0 C \\ 0 \\ 0 \end{bmatrix}. \tag{3.13}$$

Physically, this equilibrium line represents the location in the manifold spanned by the state vector with the minimum total system energy. Since the location of the current sheet, $x_1(t)$, does not affect the system energy, it can be located anywhere. The next value in the vector, $V_0 C$, corresponds with the point at which all charge initially on the capacitor has left. The last two values correspond to states of no kinetic energy or circuit energy. Based on this physical interpretation and with the knowledge the system satisfies energy conservation through the circuit equation, this equilibrium point should be stable.

### 4.2.1.     Reachability

The notion of reachability addresses the capability of a system's input actuators to bring the system to a different state. In other words, given the correct choice of input, what can be said about the set of points that can be reached from the initial state in a finite time [Nijmeijer et al., 1990]. For the goals of this study, in increasing the exhaust velocity state, this question is critical. For nonlinear systems, several statements of

72

reachability exist, however, all of them are of local nature due to their inclusion of a linearization of the system. This is due to the fact that, for a nonlinear system, a 'large' distance or a 'long' time may be required in order to reach points near some initial state [Casti, 1985]. In addition to this local description, nonlinear systems also have reachability specified as either strong or weak. The concept of strong reachability contrasts with weak reachability in that, it provides for a symmetric statement of reachability. That is, in weak reachability, some state may be reachable from some initial state, but the converse would not be true, while in strong reachability, the states are both reachable from each other. The reachability test conducted in this study, which provides a statement of the system's locally strong reachability, is found in Nijmeijer et al. [1990]. Like all statements of controllability and reachability, a relatively simple, albeit lengthy, algebraic test, leads to a statement of a nonlinear system's locally strong reachability. This test involves the calculation of the determinant of the systems strong accessibility algebra. If the determinant is nonzero, the input vectors contained within the strong accessibility algebra are linearly independent, span $\mathbb{R}^n$ and the system is locally strongly accessible.

$$\det\left(C_0\right) \neq 0 \tag{3.14}$$

The strong accessibility algebra is given by

$$C_0 = \left[\mathbf{g}_1, \overline{\mathbf{g}}_2, \overline{\mathbf{g}}_3, \overline{\mathbf{g}}_4\right], \tag{3.15}$$

where

$$\overline{\mathbf{g}}_2 = [\mathbf{g}_1, [\mathbf{f}, \mathbf{g}_1]_{LB}]_{LB}, \quad \overline{\mathbf{g}}_3 = [\overline{\mathbf{g}}_2, [\mathbf{f}, \mathbf{g}_1]_{LB}]_{LB}, \quad \overline{\mathbf{g}}_4 = [\overline{\mathbf{g}}_3, [\mathbf{f}, \mathbf{g}_1]_{LB}]_{LB}. \tag{3.16}$$

The brackets in (3.16) represent Lie bracket operations. These Lie bracket calculations were found to be quite tedious for the PPT system, therefore MAPLE® was utilized to perform them.

The result of this reachability test was that the system was found to be locally strongly accessible as long as the velocity $\left[ x_3(t) \right]$ and the current $\left[ x_4(t) \right]$ are not both equal to zero. This would physically make sense, as the external field would require some current or some sheet movement in order to influence the system.

# Chapter 5

# Controller Simulations

The constant open-loop controller was simulated by the modified model for the cases of the 1984 UOT PPT, the LES-6 and the LES-8/9. These thrusters represent a broad range of PPT capacitor energy levels (1.8, 20 and 125 J) and parallel plate geometries. Since each of these thrusters is ablative, the slug mass distribution model was utilized. In the case of 1984 UOT PPT the experimental mass bit data was utilized in the simulations. However, in the case of the LES-6 and LES 8/9 a constant value of mass bit was simulated. Though this is in contrast with previous UOT experimental data, which indicated an initial drop in mass bit with increasing field strength, for the purposes of these simulations it is a sufficient approximation. It should also be noted that the UOT PPTs all had propellant arrangements along the direction of the current sheet propagation. This would result in thrusters that operate predominately gas-dynamically, with large measured mass bits that would be reduced significantly with accelerating external magnetic fields. These large mass bits are indeed represented experimentally in the UOT measurements. For example, for a 14.5 J UOT PPT operating with no applied magnetic field, the mass bit was measured to be over 60 μg, compared to 28.5 μg for and LES-8/9 operating at a higher 20 J [Kimura et al., 1979]. The LES-8/9 and LES-6, with their propellant at the back of the channel, therefore, should be more 'immune' to mass bit decreases with accelerating fields.

The external field was applied up until the end of the thruster channel or at the point where the current reversal began. This later restriction results in order to apply only an accelerating external field. With a constant direction and magnitude external field, were the current to reverse with the current sheet still moving through the field, a decelerating Lorentz force would result. Accordingly, for each thruster, it is assumed this approach will maximize the effect of the controller on the exhaust velocity. For each value of magnetic field strength, an initial simulation was run with the external field applied over the entire length of the thruster channel to check for the presence of current reversal. If the current did not reverse before the sheet exhausted, this simulation would stand. However, if the current was found to reverse in the channel, the position this reversal initiated was determined. A final simulation was then run, with the external field applied up until this point. In the case of the LES-6 and LES-8/9 the mass bit utilized in each simulation

## 5.1.    1984 UOT PPT

In the 1984 UOT PPT validation simulation presented in section 3.4, the external field was applied only over the first 1.75 cm of the thruster channel. As can be seen in Figure 6.1, while this will include the current peak, there is a portion of the discharge with very high current for which an accelerating applied magnetic field is not being applied. The points in the figure represent exhaust values, while the line represents the time at which the current sheet is no longer influenced by the external magnetic field.
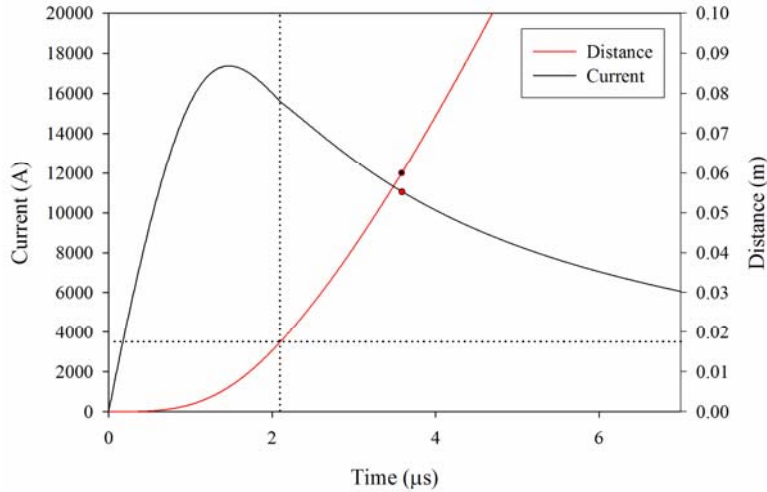
**Figure 5.1 1984 UOT PPT simulation current and distance (Bext = 0.3).**

In the present set of simulations, the external field was applied over the entire length of the thruster channel. Through this, a comparison was made between applying a magnetic field over a portion of the discharge versus the entire discharge. It should be noted that the field was applied over the entire channel length as the simulation indicated no current reversal for all cases. Figures 6.2 and 6.3 plot the comparison for specific impulse, thrust efficiency and impulse bit over applied magnetic field strength. All plots compare only simulation results.
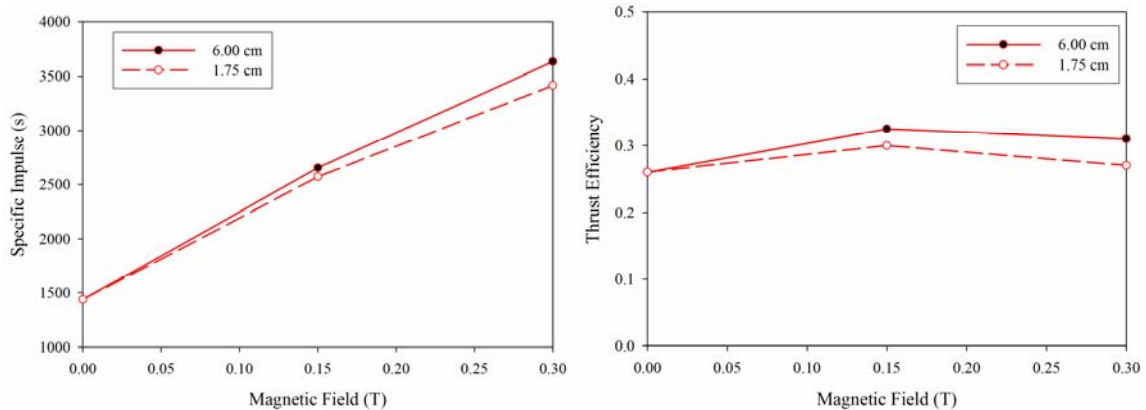


**Figure 5.2 Specific impulse and thrust efficiency comparison.**
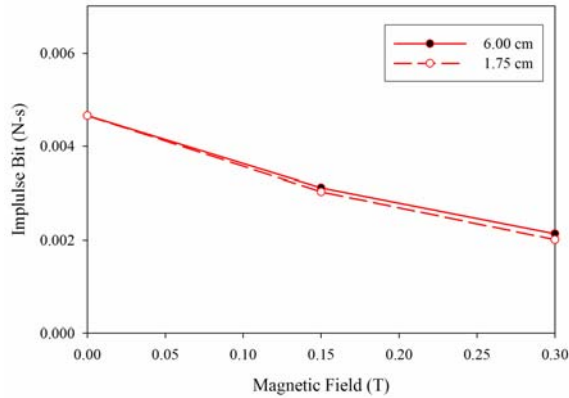
**Figure 5.3 Impulse bit comparison.**

As can be seen in these comparisons, the performance benefits increase with applied field strength. At a field strength of 0.3 T, these improvements are on the order of 10% for specific impulse and thrust efficiency, with the impulse bit showing only a slight increase. Whether these performance improvements are worthwhile would depend upon the modification needed to apply them. That, of course, would have to be answered in an analysis of the hardware needed to apply these fields, which is beyond the scope of this study.

## 5.2. LES-6

The LES-6 was simulated with accelerating applied field strengths of 0, 0.25, 0.5, 0.75 and 1.0 T. The mass bit utilized in these simulation was the experimentally measured value of 10 μg. Since, the current was found to reverse before current sheet exhaust, the external magnetic field was applied up until the point that current reversal was initiated. The following plots (Figure 6.4) display the effect of the fields on the current sheet position and velocity.
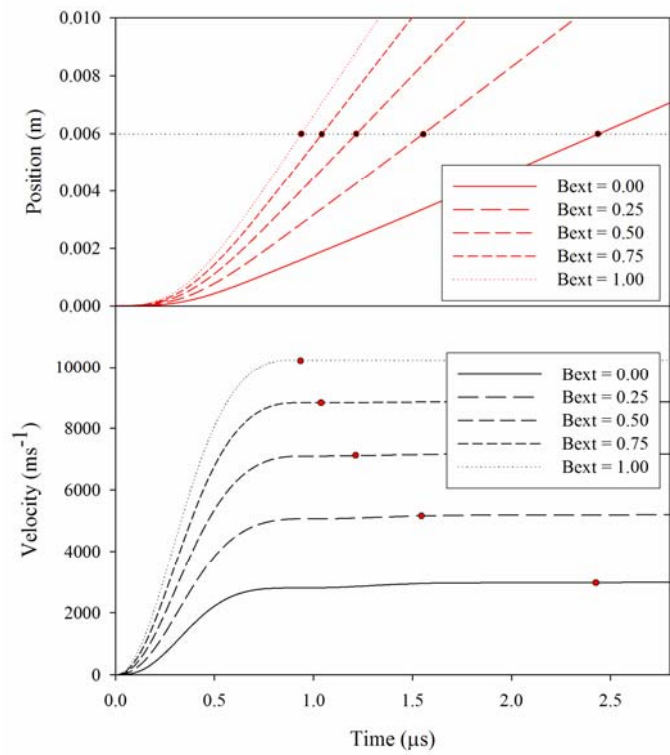
**Figure 5.4  Effects of constant magnitude externally applied magnetic fields on**

**current sheet position and velocity for the LES-6.**

As can be seen in Figure 6.4, by increasing the field strength, the exhaust velocity of the thruster can be increased.  However, this effect appears to diminish with increasing field strength.   The current and voltage waveforms are significantly modified by the emf generated by the applied magnetic field.   The following plots (Figure 6.5) show this effect.
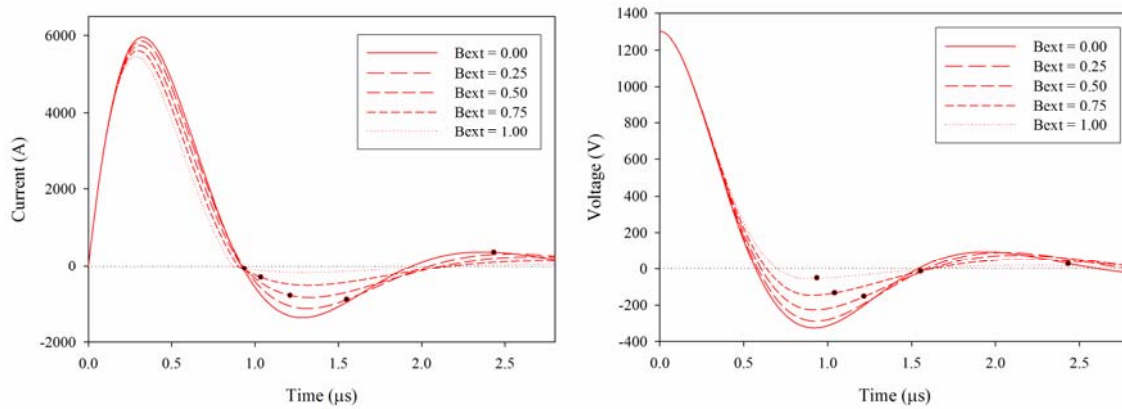
**Figure 5.5  Effects of constant magnitude externally applied magnetic fields on current and capacitor voltage for the LES-6.**

As can be seen in the current waveforms, for all magnitudes of applied field, current reversal occurs.  For 0.75 and 1.0 T, however, this reversal is small and near the exit of the thruster.  Both the current and voltage waveforms exhibit a trend of decreasing amplitude with increasing applied magnetic field strength.  This effect on current was observed in the UOT experiments [Kimura et al., 1979] and is most likely due to the emf generated by the applied field in the PPT circuit.  Figure 6.6 shows the performance enhancements of externally applied magnetic fields.
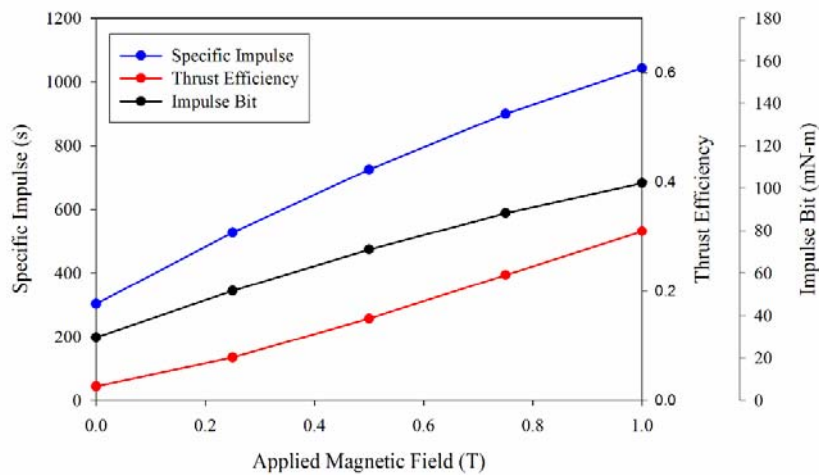


**Figure 5.6  Effects of accelerating magnetic fields on LES-6 performance.**

These plots show significant performance enhancements with increasing externally applied accelerating magnetic fields. Each performance term increases approximately linearly as field strength, with the specific impulse increasing 740 s per Tesla, the thrust efficiency increasing 28 % per Tesla and the impulse bit increasing 72 μN-s per Tesla.

## 5.3. LES-8/9

Like the LES-6, the LES-8/9 was also simulated with accelerating applied field strengths of 0, 0.25, 0.5, 0.75 and 1.0 T. As will be seen in figure 5.8, the simulation predicted no current reversal for all applied field strengths and so the field was applied over the entire length of the channel. The plots in Figure 6.7 display the effects of the fields on the current sheet position and velocity.
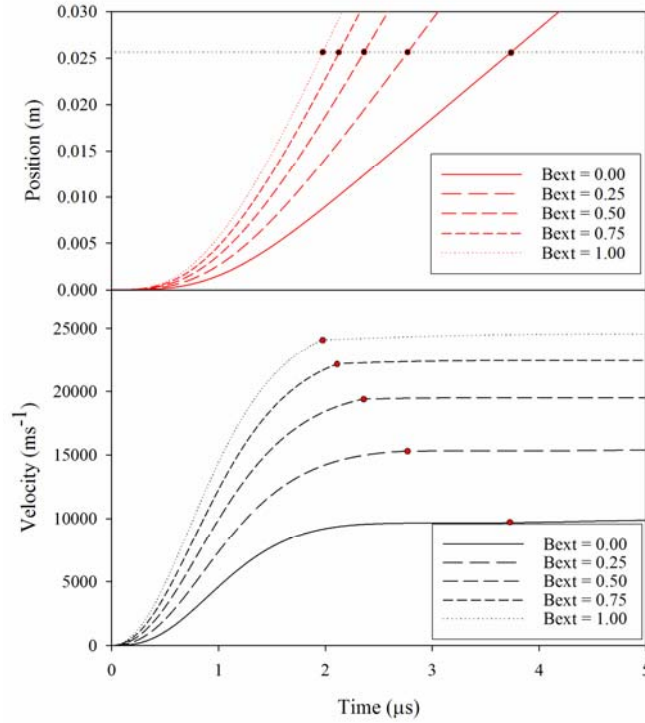
**Figure 5.7  Effects of constant magnitude externally applied magnetic fields on current sheet position and velocity for the LES-8/9.**

The effects here are virtually the same as for the LES-6.  The current and voltage waveforms displayed in Figure 6.8 show the same characteristics as the LES-6, with diminished peak amplitude.
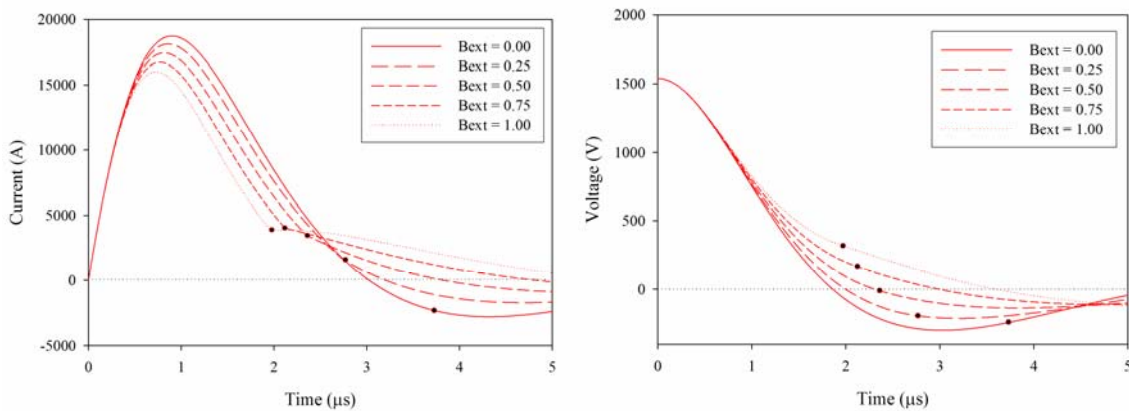


**Figure 5.8  Effects of constant magnitude externally applied magnetic fields on current and capacitor voltage for the LES-8/9.**

As can be seen in these current waveforms, there was no current reversal for any of the cases with applied magnetic fields. Figure 6.9 displays the performance enhancements of externally applied magnetic fields in this thruster.
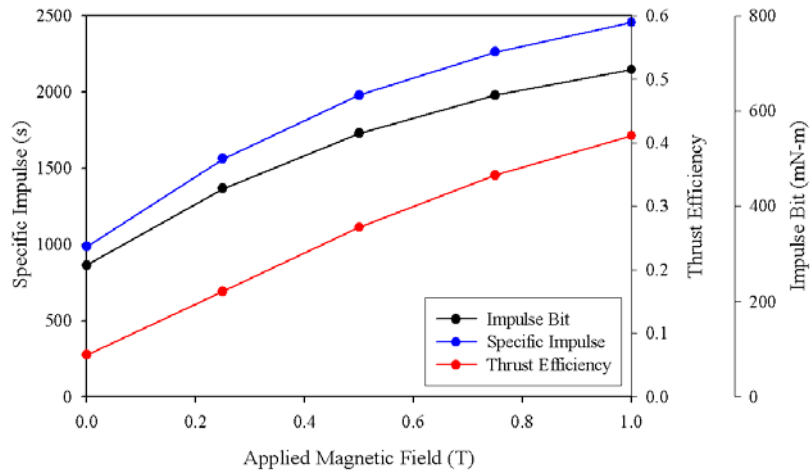


**Figure 5.9  Effects of accelerating magnetic fields on LES-8/9 performance.**

These plots (Figure 6.9) show significant performance enhancements with increasing externally applied accelerating magnetic fields.  Each performance term increases approximately linearly as field strength, with the specific impulse increasing 1471 s per Tesla, the thrust efficiency increasing 34 % per Tesla and the impulse bit increasing 411 μN-s per Tesla.

# Chapter 6

# Conclusions and Recommendations

The work in this thesis was devoted to the development of a flow-control strategy aimed at increasing the performance of PPTs. This strategy explored the use of externally applied magnetic fields as actuators to bring the PPT system to a higher exhaust velocity and thus improved performance state. The strategy employed the use of a one dimensional model of PPT operation and so significant emphasis was placed on the derivation and validation of this model. The model was validated for the case of parallel plate APPTs, by comparison with LES-6 and LES-8/9 experimental data. To simulate the controller a modified version of this validated model was derived and implemented. This modified model was itself validated for the case of a constant magnitude external magnetic field by comparison with experiments conducted at the UOT. Finally, the proposed open-loop controller was simulated for the cases of the LES-6, the LES-8/9 and a UOT thruster.

## 6.1.    Model Contributions, Analysis and Results

The general PPT model utilized throughout this work was similar to those appearing previously in literature but included a mass distribution model and a plasma resistance model. The mass distribution model, appearing in Michels et al. (1966), was employed as a convenient way to accommodate for variable mass distributions throughout the thruster channel ranging from slug to snowplow. The plasma resistance

model, included in this work, was novel for one dimensional PPT modeling and was based on the Spitzer plasma conductivity. In the modified model, the inclusion of an external magnetic field, applied to the parallel-plate geometry, was likewise novel. In this study, a time-variant magnetic field with negligible spatial gradient throughout the channel was modeled.

A controls analysis was conducted examining the controllability of the modified model. To assess controllability, the case of a constant applied magnetic field input was examined. This nonlinear system was found to be controllable as long as the system exhibited some current or current sheet velocity. For $t > 0$, a discharging PPT would physically always satisfy this requirement.

An open-loop controller based on this system was simulated for use on the LES-6, the LES-8/9 and the UOT PPT. The UOT simulation was a comparison of applying an accelerating external magnetic field over the full length of the channel (6.0 cm) versus a partial length (1.75 cm). The simulations showed that, despite an increase in performance, these enhancements were only on the order of, at most, 10%. This indicates that a majority of the performance improvement could be realized by applying a field only over an initial section of the thruster channel.

The LES-6 and LES-8/9 simulations explored the general benefits realized by applying constant magnitude external magnetic fields. These fields were applied over the full length of the thruster channel, as long as current reversal did not occur before exhaust. For the LES-6, the external field was applied only over a partial length of the thruster channel due to current reversal. This length terminated at the point current reversal occurred and varied with the external field strength applied, increasing with

increasing field strength. The LES-8/9 simulation did not display such current reversal conditions in the channel and so the magnetic field was applied over the full length of the channel.

Both the LES-6 and LES-8/9 simulations showed significant linear increases in performance with increasing applied field strength. For the LES-6, these rates of performance increase were 740 s per Tesla for specific impulse, 28 % per Tesla for thrust efficiency and 72 μN-s per Tesla for the impulse bit. For the LES-8/9, the rates of performance increase were 1471 s per Tesla for the specific impulse, 34 % per Tesla for the thrust efficiency and 411 μN-s per Tesla for the impulse bit. While these enhancements are significantly large, they are of similar order of magnitude to improvements measured in the UOT applied field PPT experiments [Kimura, 1979].

## 6.2. Recommendations and Directions for Further Research

The main areas of recommendations for future research pertain to both theoretical and experimental work. The recommendations for future theoretical work includes examining variable open-loop and close-loop controllers and to perform a systems study examining applied magnetic field PPT implementation on microspacecraft. The recommendations for future experimental research pertains to a continuation of the work performed at the UOT in investigating applied magnetic field PPTs.

With constant open-loop control having been examined in this work, the next step would be to investigate variable open-loop controllers and close-loop (feedback) controllers. The examination of feedback controller should be accompanied by an analysis of the modified model that includes the second input term. Additionally, a study

86

addressing the feasibility of real-time application of feedback controllers should be conducted.

A systems study investigating actual implementation of applied magnetic field thrusters on spacecraft, particularly on microspacecraft, should be conducted. A study of this nature has never been performed for applied field magnetic field PPTs and would consider if the performance improvements of these PPTs warrant the penalties of added mass and power. Specifically, the increase in dry mass of an applied magnetic field PPT should be compared with the decrease in necessary propellant mass, which results from an increase in specific impulse. Furthermore, if electromagnets are to be utilized in generating the external field, a thrust efficiency including external circuit energy must be examined.

A study involving a real applied magnetic field PPT would, naturally, provide the ideal investigation of these thrusters. This type of experimental work is warranted by more than just the results of this thesis. The parallel plate PPT experiments conducted at UOT, while displaying the feasibility of implementing externally applied magnetic fields to parallel plate PPTs, also showed the significant performance enhancements realized by these fields. Like the UOT group, both permanent and electromagnet investigations should be conducted aimed at confirming the simulation results presented in this work and the UOT experimental results.

# Appendix A

# External Circuit Modified Models

Though the case of an external circuit was not investigated in this study, the following model derivations are for this case. The two external circuits being examined in this appendix describe, respectively, the PPT circuit coupled with an external LCR circuit (figure 4.3) and the PPT circuit coupled with external LR circuit with a controllable voltage supply (figure 4.4). For these derivations the subscript 1 and 2 refer to the PPT circuit and external circuit, respectively.

The circuit equation describing the PPT circuit coupled with the external LCR circuit begins with a statement of Faraday's law for each circuit.

$$V_{c_1}(t) = I_1 R_{T_1}(t) + \frac{d}{dt}[\lambda_1],$$
(A.1)

$$V_{c_2}(t) = I_2 R_{T_2}(t) + \frac{d}{dt}[\lambda_2].$$
(A.2)

These equations may be expanded as

$$V_{c_1}(t) - I_1 R_{c_1} - I_1 R_e - I_1 R_p = L_{c_1} \dot{I}_1 + L_e \dot{I}_1 + \frac{d}{dt}[\lambda_{pe}],$$
(A.3)

$$V_{c_2}(t) - I_2 R_{c_2} = L_{c_2} \dot{I}_2 + \frac{d}{dt}[\lambda_y],$$
(A.4)

where $\lambda_{pe}$ is the magnetic flux through the PPT circuit plate electrodes and $\lambda_y$ is the magnetic flux through the external circuit yoke. Assuming the external circuit coils around the yoke as an $N$-turn very long cylindrical solenoid, these two terms may be written as

$$\lambda_{pe} = \mu_0 \frac{h}{w} x_s I_1 + \mu_0 \frac{N^2 A}{d} \frac{x_s}{l} I_2, \tag{A.5}$$

$$\lambda_y = \mu_0 \frac{h}{w} x_s I_1 + \mu_0 \frac{N^2 A}{d} I_2, \tag{A.6}$$

where $A$ and $d$ represent, respectively, the cross sectional area of the loops and the total length of the coil. Substituting (A.5) and (A.6) into equations (A.3) and (A.4) yields

$$V_{0_1} - \int_0^t I_1(\tau) d\tau - \left( R_{c_1} + R_e + R_p \right) I_1 = \left( L_{c_1} + L_e \right) \dot{I}_1 + \mu_0 \frac{h}{w} \left( \dot{x}_s I_1 + x_s \dot{I}_1 \right) + \mu_0 \frac{N^2 A}{d} \left( \frac{\dot{x}_s}{l} I_2 + \frac{x_s}{l} \dot{I}_2 \right)$$
$$\text{(A.7)}$$

$$V_{0_2} - \int_0^t I_2(\tau) d\tau - I_2 R_{c_2} = L_{c_2} \dot{I}_2 + \mu_0 \frac{h}{w} \left( \dot{x}_s I_1 + x_s \dot{I}_1 \right) + \mu_0 \frac{N^2 A}{d} \dot{I}_2. \tag{A.8}$$

The external circuit equation, (A.8) requires an additional two boundary conditions for the external LCR circuit PPT system to be fully stated. These initial conditions would depend upon how the external circuit would be operated, however, for the case that both circuits are discharged at the same time, the following initial conditions would be implemented,

$$\int_0^{t=0} I_2(\tau) = 0, \ I_2(0) = 0. \tag{A.9}$$

The above two equations (A.7) and (A.8) and these initial conditions are the only modifications to the general model introduced by coupling an external LCR circuit to the PPT system.

For the case of a controllable voltage source, the same exact derivation would follow, with the only divergence in the final external circuit equation (A.8) and initial conditions

$$V = L_{c_2}\dot{I}_2 + \mu_0 \frac{h}{w}\left(\dot{x}_s I_1 + x_s \dot{I}_1\right) + \mu_0 \frac{N^2 A}{d}\dot{I}_2,$$
(A.10)

where $V$ is the voltage of the controllable voltage source. Since this equation is a first order differential equation, only one boundary condition is required

$$I_2(0) = 0.$$
(A.11)

# References

Burton, R.L., Turchi, P.J., "Pulsed Plasma Thruster," *Journal of Propulsion and Power*, Vol. 14, No. 5, September-October 1998, pp. 716-735.

Burton, R.L., Wilson, M.,J., Bushman, S.,S., "Energy Balance and Efficiency of the Pulsed Plasma Thruster", AIAA-1998-3808, 34th Joint Propulsion Conference, Cleveland, OH, July 1998.

Butler, T.D., Henins, I., Jahoda, F.C., Marshall, J., Morse, R.L., "Coaxial Snowplow Discharge," *The Physics of Fluids*, Vol. 12, No. 9, 1969, pp. 1904-1916.

Campbell, M., Ruckner, A.P., Hwee, G., Ewig, R., Kaltenbach, S., Beltran, E., Lai, G., Carlson, E., Nadkarni, A., Parker, K., Carpenter, K., Peyton, M., Chung, S., Pillar, S., Davenport, B., Shell, W.M., Forouhar, F., Titus, D., Halligan, J.K., Tucker, M., Hammack, J., Vlachos, A., Hilstad, M.,"UW Dawgstar: One Third of ION-F," SSC9-III-4, *Proceedings of the 13th AIAA/USU Conference on Small Satellites*, Logan, UT, 23-26 August 1999.

Casti, J.L., Nonlinear System Theory: Mathematics in Science and Engineering, Vol. 175, Academic Press, Inc., Florida, 1985, Chapter 4.

Cobb, R. "Techsat 21, Space Missions Using Distributed Micro-Satellite Systems," University Satellite Kickoff Meeting, January 1999.

Dormand, J.R. and P.J. Prince, "A Family of Embedded Runge-Kutta Formulae," Journal of Computational and Applied Mathematics, Vol. 6, 1980, pp. 19-26.

Gagne, M., "Triple Langmuir Probe Measurements and Numerical Modeling of Gas-Fed Pulsed Plasma Thruster Plumes," M.S. Thesis, Worcester Polytechnic Institute, Department of Mechanical Engineering, Worcester, MA, May, 2000.

Gatsonis, N.A., DeMagistris, M., Erlandson, R.E., "Three-Dimensional Magnetohydrodynamic Modeling of Plasma Jets in North Star Space Experiment", *Journal of Spacecraft and Rockets*, Vol. 41, No. 4, 2004, pp. 509-520.

Gatsonis, N.A., Demetriou, M.A., "Prospects of Plasma Flow Modeling and Control for Micro Pulsed Plasma Thruster," AIAA-2004-3464, 40th Joint Propulsion Conference, July 11-14, 2004.

Hart, P.J., "Plasma Acceleration with Coaxial Electrodes," *The Physics of Fluids*, Vol. 5, No. 1, January 1962.

Haus, A.H., Melcher, J.R., Electromagnetic Fields and Energy, Prentice-Hall, Englewood Cliffs, New Jersey, 1989, Chapters 1, 8 and 10.

Jahn, R. G., Choueiri, E.Y., "Electric Propulsion," *Encyclodpedia of Physical Science and Technology*, 3rd Edition, Academic Press, San Diego, v.5, pp125-141, 2002.

Jahn, R.G., Physics of Electric Propulsion, McGraw-Hill, New York, 1968, Chapter 9.

Johnson, L., Bromaghim, D., "AFRL-0302 - Microsatellite Propulsion Integration (MPI)," Deparment of Defense Space Experiments Review Board (SERB) Presentation, November 4-6, 2003.

Leiweke, R.J., "An Advanced Pulsed Plasma Thruster Design Study Using One-Dimensional Slug Modeling," AFOSR Summer Research Program Final Report, Phillips Laboratory, Kirkland Air Force Base, New Mexico, January 1996.

Michels, C.J., Heighway, J.E., Johansen, A.E., "Analytical and Experimental Performance of Capacitor Powered Coaxial Plasma Guns," *AIAA Journal*, Vol. 4, No., 5, May 1966.

Mikellides, P.G., Turchi, P.J., "Modeling of Ablation-Fed Pulsed Plasma Thrusters," AIAA-1995-2915, 31nd Joint Propulsion Conference, San Diego, CA, July 10-12, 1995.

Mitchner, M., Kruger, C.H., Partially Ionized Gases, John Wiley & Sons, Inc., Indianapolis, IN, 1973, Chapter 2.

Mueller, J., "Thruster Options for Microspacecraft: A Review and Evaluation of the State-of-the-Art and Emerging Technologies", Micropropulsion for Small Spacecraft, Progress in Astronautics and Aeronautics, Vol. 187, 2000, Chapter 3.

Myers, R.M., Oleson, S.R., Curran, F.M., Schneider, S.J., "Small Satellite Propulsion Options", AIAA-94-2997, 30th Joint Propulsion Conference, Indianapolis, IN, June 1994.

Nijmeijer H., Van der Schaft, A., Nonlinear Dynamical Control Systems, Springer-Verlag, New York, 1990, Chapter 3.

Pollard, J.E., Jackson, D.E., Marvin, D.C., Jenkin, A.B., Janson, S.W., "Electric Propulsion Flight Experience and Technology Readiness," 29th Joint Propulsion Conference and Exhibit, Monterey, CA, June 28-30, 1993.

Rayburn, C. D., Campbell, M. E., Mattick T. A., "Pulsed Plasma Thruster System for Microsatellites," *Journal of Spacecraft and Rockets*, Vol. 42, No. 1, pp. 161-170, 2005.

Vondra R., Thomassen, K., Solbes, A., "A Pulsed Electric Thruster for Satellite Control," Proceedings of the IEEE, Vol. 59, No. 2, February 1971, pp. 271-277.

Vondra, R.J., Thomassen, K., Solbes, A., "Analysis of Solid Teflon Pulsed Plasma Thruster," *Journal of Spacecraft and Rockets*, Vol. 7, No.12, 1970, pp. 1402-1406.

Waltz, P.M., "Analysis of a Pulsed Electromagnetic Plasma Thruster," M.S. Thesis, Massachusetts Institute of Technology, Department of Electrical Engineering, Cambridge, MA, 1969.

Ziemer, J. K., Cubbin, E. A., Choueiri, E.Y., "Performance Characterization of a High Efficiency Gas-Fed Pulsed Plasma Thruster," AIAA-97-2925, Presented at the 33rd Joint Propulsion Conference, Seattle, WA, July 6-9, 1997.

Ziemer, J.K., Choueiri, E.Y., "A Characteristic Velocity for Gas-Fed PPT Performance Scaling", AIAA-2000-3432, 36th Joint Propulsion Conference, Huntsville, AL, July 16-20, 2000.

Ziemer, J.K., Choueiri, E.Y., "Dimensionless Performance Model for Gas-Fed Pulsed Plasma Thrusters," AIAA-98-3661, 34th Joint Propulsion Conference, Cleveland OH, July 14-17, 1998.

Ziemer, J.K., Choueiri, E.Y., "Scaling Laws for Electromagnetic Pulsed Plasma Thrusters," Plasma Sources Science and Technology, Vol 10, No. 3, August 2001, pp. 395-405.

Ziemer, J.K., Choueiri, E.Y., Birx, D., "Trends in Performance Improvements of a Coaxial Gas-Fed Pulsed Plasma Thruster," IEPC-97-040, 25th International Electric Propulsion Conference, Cleveland, OH, August 24-28, 1997.